Control of ultrafast electron dynamics with shaped femtosecond laser pulses: from atoms to solids

Matthias Wollenhaupt[1], Tim Bayer[1] and Thomas Baumert[2]

[1]Carl von Ossietzky Universität Oldenburg, Institut für Physik, Carl-von-Ossietzky-Straße 9-11, D-26129 Oldenburg Germany,
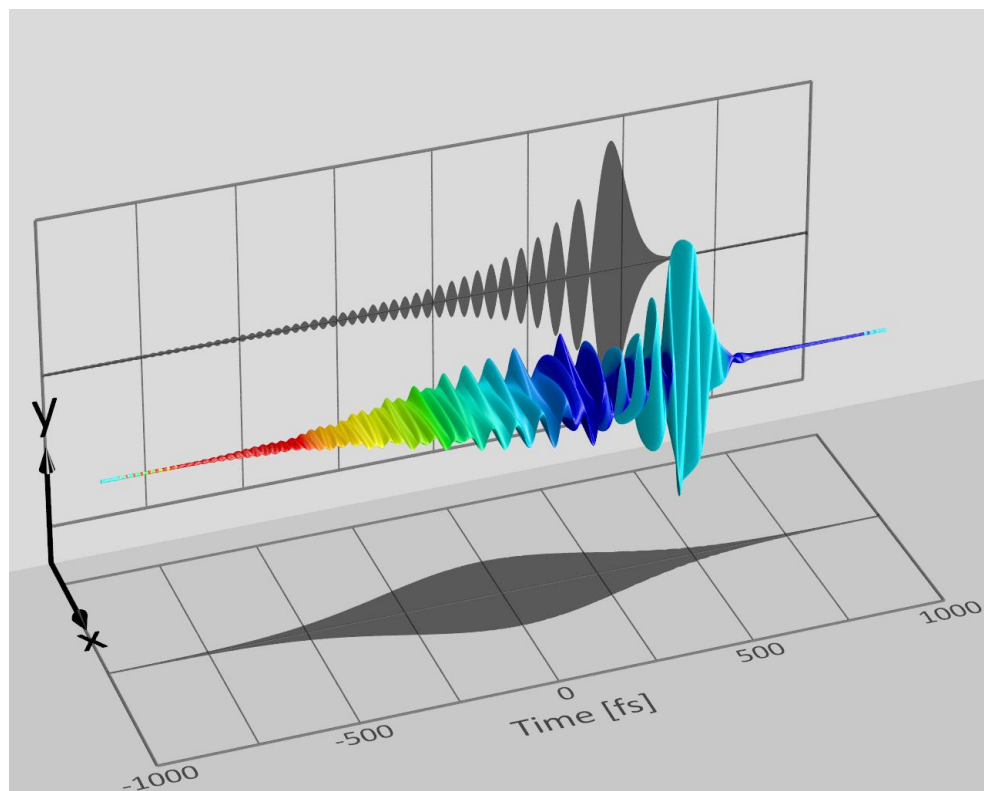
E-Mail: matthias.wollenhaupt@uni-oldenburg.de

E-Mail: tim.bayer@uni-oldenburg.de

[2]Universität Kassel, Institut für Physik und CINSaT, Heinrich-Plett-Str. 40,

D- 34132 Kassel, Germany. Fax:+49 561 804 4453,

E-mail: baumert@physik.uni-kassel.de

1. Introduction

In coherent control shaped femtosecond laser pulses are used as a tool to steer the ultrafast light-induced dynamics of a quantum system from a given initial state to a predefined target state, preferably with high selectivity and high efficiency. Progress in this fast expanding research field is reported in recent text books [1-3], review articles [4-23] and special issues [24-29]. In this review, we focus on advanced control of ultrafast electron dynamics with shaped femtosecond laser pulses investigated by photo-ionization. In the studies presented, the role of photo-ionization is twofold: on the one hand, the details of the photo-ionization dynamics are explored, whereas, on the other hand, photoelectron spectra are employed as a powerful tool to monitor the controlled neutral dynamics.

A deeper understanding of the principles of pulse shaping and the ability to generate shaped femtosecond pulses with high precision in the laboratory are two important prerequisites to successfully carry out coherent control experiments. Therefore, we start this chapter with an introduction to the theoretical and experimental fundamentals of pulse shaping and elaborate on control of the time-dependent polarization profile of a femtosecond laser pulse, in addition to its temporal envelope and phase. Before we present some recent applications, we will clarify the essential concepts of polarization shaping including a characterization of the instantaneous frequency and the instantaneous polarization state and present several prototypical examples.

Because the emphasis of this review is placed on understanding the physical mechanisms of coherent control, we mainly focus our attention on isolated model systems in the gas phase. Since the physical basis of coherent control is the manipulation of the interferences of matter waves by laser radiation, we will start by investigating the transfer of the coherence properties from laser pulses to matter waves. To this end, we study the photoionization of potassium atoms with a phase-coherent double pulse sequence. Building on this simple example we discuss creation and measurement of three dimensional designer free electron wave packets as an example for complex but still comprehensible control by polarization-shaped pulses. In addition, two examples of adaptive optimization of photoionization processes by polarization-shaped femtosecond

laser pulses are reported. New physical mechanisms to exert efficient control become available when intense femtosecond laser pulses are used. The non-perturbative interaction with shaped pulses entails novel dynamics such as complete population transfer, Rabi-oscillations or Photon Locking (see below) which are unavailable in weak fields and thus opens numerous novel control scenarios. We will portray some prototype examples highlighting specific control mechanisms such as non-resonant dynamic Stark shifts and bipolar energy shifts through resonant excitation. We introduce the concept of control by selective population of dressed states (SPODS) which is particularly suited to describe strong field interactions and provides a unified perspective on adiabatic techniques and ultrafast switching by phase jumps. Applying these techniques to selective excitation of molecules opens the fascinating subject of coherent control of the concerted nuclear and electronic dynamics which concludes the section on strong-field control. Finally, we present a short overview on recent work on control of ionization processes in dielectrics with applications in nano- materials processing.

2. Fundamentals of femtosecond pulse shaping

In this introductory section we present the fundamentals of femtosecond pulse shaping in view of the applications discussed in this chapter, such as photo-ionization of atoms and molecules as well as material processing. In this theoretical section a mathematical description of femtosecond pulse shaping is presented along with basic definitions and relevant equations. Special emphasis is placed on polarization shaping which plays a central role in the creation of designer electron wave packets. In addition, the closed loop approach to find optimal laser pulses by adaptive feedback learning is summarized and a brief description of the experimental implementation of a liquid crystal based 4f pulse shaper used in these experiments is given.

2.1. Theoretical description

In this section we introduce the basic physical quantities of the laser electric field which are required to understand the properties of shaped pulses [20,30,31]. We will concentrate on pulse shaping by spectral phase modulation with applications to control of ultrafast electron dynamics. Polynomial phase functions such as GDD and TOD and pulse trains created by sinusoidal phase modulation are investigated in

some detail. In addition, we discuss spectral phase functions resulting from the combined action of two different modulation functions. The pulse duration is a central quantity to characterize femtosecond pulses and to classify the interaction in terms of the relevant physical time scales. Therefore, we generalize this concept towards shaped laser pulses and introduce statistical quantities based on the moments of the temporal pulse intensity distribution as a quantitative measure for the duration of a shaped pulse. A practical analytic expression for determining the pulse duration in frequency domain only using the spectral phase function is given. As a reference, analytic expressions for the temporal field envelopes and the corresponding pulse durations of the relevant shaped pulses are provided.

2.1.1. Definition of the physical quantities

We start by considering the linearly polarized real-valued time-dependent pulsed laser electric field (in units of Vm^{-1})

$$E(t) = A(t) \cos[\omega_0 t + \zeta(t)] \tag{1}$$

oscillating with the carrier frequency ω_0. Here, $A(t)$ is the real valued envelope of the field and the temporal phase function $\zeta(t)$ denotes slowly varying temporal phase changes. Physically, the temporal phase function is responsible for variations in the instantaneous frequency, for instance frequency sweeps or phase discontinuities in pulse sequences. Defining the time-dependent detuning $\Delta(t)$ by the derivative of the temporal phase function

$$\Delta(t) = \frac{d\,\zeta(t)}{dt} \tag{2}$$

the instantaneous frequency $\omega(t)$ is given by the sum of the laser central frequency and the time-dependent detuning

$$\omega(t) = \omega_0 + \Delta(t). \tag{3}$$

Defining the slowly varying – and in general complex valued – function

$$\mathcal{E}(t) = A(t)e^{i\,\zeta(t)} \tag{4}$$

which is called the complex pulse envelope, Equation (1) can be rewritten as

$$E(t) = Re[\mathcal{E}(t)\,e^{i\,\omega_0 t}] = \frac{1}{2}[\mathcal{E}(t)\,e^{i\,\omega_0 t} + \mathcal{E}^*(t)\,e^{-i\,\omega_0 t}], \tag{5}$$

where the symbol (*) denotes complex conjugation.

In general, the analytic signals $\mathcal{E}^+(t)$ and $\mathcal{E}^-(t)$ are introduced to characterize ultrashort shaped laser pulses [30]. However, since the SVEA (Slowly Varying

Envelope Approximation) applies for the pulses considered here, the envelope function $\mathcal{E}(t)$ defined by Equation (4) is sufficient to describe the electric field. Combining the Equations (3) and (5) provides a useful expression to derive the instantaneous detuning directly from the complex envelope without resorting to inverse trigonometric functions and hence avoiding phase ambiguities [32]

$$\Delta(t) = \frac{i}{2}\frac{\mathcal{E}(t)\frac{d}{dt}\mathcal{E}^*(t) - \mathcal{E}^*(t)\frac{d}{dt}\mathcal{E}(t)}{\mathcal{E}(t)\,\mathcal{E}^*(t)} = -\frac{\mathrm{Im}\left[\mathcal{E}(t)\frac{d}{dt}\mathcal{E}^*(t)\right]}{|\mathcal{E}(t)|^2}, \tag{6}$$

where Im denotes the imaginary part and hence, $\Delta(t)$ is always a real quantity. The spectrum $\tilde{E}(\omega)$ (in units of Vsm^{-1}) of the laser electric field $E(t)$ is obtained by Fourier transform of $E(t)$

$$\tilde{E}(\omega) = \int_{-\infty}^{\infty} E(t)e^{-i\omega t}\,dt. \tag{7}$$

Because the field $E(t)$ is real-valued and oscillates with the carrier frequency ω_0, its spectrum is Hermitian $\tilde{E}(-\omega) = \tilde{E}^*(\omega)$ and has non-vanishing contributions only around $\omega = +\omega_0$ and $\omega = -\omega_0$. Analogously, the Fourier spectrum $\widetilde{\mathcal{E}}(\omega)$ (also in units of Vsm^{-1}) of the complex valued envelope $\mathcal{E}(t)$ is given by

$$\widetilde{\mathcal{E}}(\omega) = \int_{-\infty}^{\infty} \mathcal{E}(t)e^{-i\omega t}\,dt \tag{8}$$

and has only non-vanishing components around $\omega = 0$. For instance, the Gaussian

$$\mathcal{E}(t) = \frac{\mathcal{E}_0}{2}e^{-\ln 4\left(\frac{t}{\Delta t}\right)^2} \tag{9}$$

is a typical example of an unmodulated pulse envelope with an intensity FWHM (Full Width at Half Maximum of the intensity envelope $I(t) \propto \mathcal{E}^2(t)$) of Δt. The corresponding spectrum of the amplitude reads

$$\widetilde{\mathcal{E}}(\omega) = \frac{\mathcal{E}_0\,\Delta t}{2}\sqrt{\frac{\pi}{\ln 4}}\,e^{-\ln 4\left(\frac{\omega}{\Delta\omega}\right)^2}, \tag{10}$$

where the intensity FWHM of the spectrum is

$$\Delta\omega = \frac{4\ln 2}{\Delta t} \tag{11}$$

in accordance with the FWHM-bandwidth product for a Gaussian laser pulse

$$\Delta\nu\,\Delta t = \frac{\Delta\omega\,\Delta t}{2\,\pi} = \frac{4\ln 2}{2\,\pi} \approx 0.44\,. \tag{12}$$

2.1.2. Spectral modulation

Because femtosecond laser pulses are too short to be directly shaped in the

time domain they are modulated in the frequency domain applying a linear spectral transfer function $\widetilde{M}(\omega)$ (see section 2.2 for the experimental implementation of this approach). The modulated spectrum $\widetilde{\mathcal{E}}_{mod}(\omega)$ of the shaped pulse is obtained by multiplication of the spectral modulation function $\widetilde{M}(\omega)$ with the initially unmodulated spectrum

$$\widetilde{\mathcal{E}}_{mod}(\omega) = \widetilde{M}(\omega)\,\widetilde{\mathcal{E}}(\omega). \tag{13}$$

Inverse Fourier transform of the whole Equation (13) shows that the modulated complex-valued temporal field envelope $\mathcal{E}_{mod}(t)$ is obtained by convolution with the temporal modulation function

$$\mathcal{E}_{mod}(t) = \mathcal{M}(t) \otimes \mathcal{E}(t), \tag{14}$$

where the modulation functions $\mathcal{M}(t)$ and $\widetilde{M}(\omega)$ are a Fourier pair and $\otimes$ denotes the convolution. In most cases, however, it is more practical to evaluate the expression for the modulated spectrum $\widetilde{\mathcal{E}}_{mod}(\omega)$ in Equation (13) and derive the shaped pulse in time domain directly from $\widetilde{\mathcal{E}}_{mod}(\omega)$ by inverse Fourier transform

$$\mathcal{E}_{mod}(t) = \frac{1}{2\pi}\int_{-\infty}^{\infty}\widetilde{\mathcal{E}}_{mod}(\omega)\,e^{i\,\omega\,t}d\omega. \tag{15}$$

In general, the spectral modulation function can be decomposed into a spectral amplitude modulation function $\tilde{\mathcal{R}}(\omega)$ and a spectral phase modulation function $\varphi(\omega)$ by

$$\widetilde{M}(\omega) = \tilde{\mathcal{R}}(\omega)e^{-i\,\varphi(\omega)}. \tag{16}$$

Some pulse shapes – such as double pulses [33-35] - require amplitude modulation leading to an attenuation of the laser beam. In all conventional implementations of pulse shaping the amplitude modulation function fulfils the condition $\left|\tilde{\mathcal{R}}(\omega)\right| \leq 1$ because linear spectral filters only allow for attenuation of spectral components. For pure phase modulation by optically transparent spectral filters, when none of the spectral amplitudes is attenuated ($\tilde{\mathcal{R}}(\omega) \equiv 1$), one obtains the basic relation of spectral phase modulation

$$\widetilde{\mathcal{E}}_{mod}(\omega) = \widetilde{\mathcal{E}}(\omega)e^{-i\,\varphi(\omega)}. \tag{17}$$

Physically it is clear, that in the case of pure phase modulation the pulse energy is conserved. Formally, this also follows by applying Parseval's theorem (see for example [36]) to the modulated field

$$\int_{-\infty}^{\infty}|\mathcal{E}_{mod}(t)|^2 dt = \frac{1}{2\pi}\int_{-\infty}^{\infty}\left|\widetilde{\mathcal{E}}_{mod}(\omega)\right|^2 d\omega = \frac{1}{2\pi}\int_{-\infty}^{\infty}\left|\widetilde{\mathcal{E}}(\omega)\right|^2 d\omega = \int_{-\infty}^{\infty}|\mathcal{E}(t)|^2 dt$$
(18)

where we made use of the relation $\left|\widetilde{\mathcal{E}}_{mod}(\omega)\right| = \left|\widetilde{\mathcal{E}}(\omega)\right|$ for pure phase modulation. It is remarkable that in the case of phase modulation, besides the conservation of the pulse energy shown in Equation (18), the modulus of the pulse area $|\theta| = \left|\frac{\mu}{\hbar}\int_{-\infty}^{\infty}\mathcal{E}(t)\,dt\right|$ which is relevant to strong field excitation (see Section 3.3 and for example [37-39]), is also conserved. This is seen by considering

$$\theta_{mod} = \int_{-\infty}^{\infty}\mathcal{E}_{mod}(t)\,dt = \widetilde{\mathcal{E}}_{mod}(0) = \widetilde{\mathcal{E}}(0)e^{-i\varphi(0)} = e^{-i\varphi(0)}\int_{-\infty}^{\infty}\mathcal{E}(t)\,dt = e^{-i\varphi(0)}\,\theta,$$
(19)

where θ and θ_{mod} denote the pulse area of unmodulated and the modulated pulse respectively. Note that for simplicity both the dipole moment μ and Planck's constant $\hbar$ were set to unity here.

2.1.3. Combined spectral phase modulation

If a sum of multiple spectral phase functions $\varphi_i(\omega)$ is applied, the combined action of the linear combination of those phase functions can be decomposed into subsequent executions of the corresponding individual phase functions:

$$\widetilde{\mathcal{M}}(\omega) = e^{-i[\varphi_1(\omega)+\varphi_2(\omega)]} = e^{-i\,\varphi_1(\omega)}e^{-i\,\varphi_2(\omega)} = \widetilde{\mathcal{M}}_1(\omega)\,\widetilde{\mathcal{M}}_2(\omega).$$
(20)

In the time domain, the multiplication of spectral modulation functions leads to a convolution of the temporal modulation functions. For example, combining sinusoidal- and quadratic spectral phase modulation yields a sequence of chirped pulses [40] as illustrated in Figure 2(c). In general, is not always easy to predict the outcome of combinations of spectral phase functions on the temporal pulse shape due to intra-pulse interference effects of the subsequent modulations.

2.1.4. Pulse durations

The pulse duration determines the relevant physical time scale for the light matter interaction and is therefore an important experimental parameter. For an unmodulated femtosecond pulse the intensity FWHM is often used as a

quantitative measure for the pulse duration. However, the shape of phase modulated pulses is generally very complicated. For instance, shaped pulses can be temporally asymmetric, have several maxima or even consist of several distinct sub-pulses. In these circumstances, the FWHM – which is generally employed to characterize simple bell-shaped distributions – may no longer be a meaningful parameter to describe the shaped pulse. A general way to characterize the shape of a pulse by statistical methods is based on the moments of its intensity distribution. To this end, we define the shape function $f(t)$ of the pulse by

$$f(t) = \frac{\mathcal{E}(t)}{\sqrt{\int |\mathcal{E}(t)|^2 dt}} \tag{21}$$

which is independent of the pulse energy such that $f(t)$ is a normalized distribution function

$$\int_{-\infty}^{\infty} |f(t)|^2 \, dt = 1. \tag{22}$$

The nth-order moments of the modulus squared of the shape function read

$$\langle t^n \rangle = \int_{-\infty}^{\infty} t^n \, |f(t)|^2 dt. \tag{23}$$

With the above definition of the moments, one might in principle evaluate all of the higher order moments of the distribution to fully characterize the pulse. For our purpose it is sufficient to define the variance σ^2 of the function (t)

$$\sigma^2 = \langle t^2 \rangle - \langle t \rangle^2 \, . \tag{24}$$

which is a convenient measure of the statistical pulse duration of a shaped pulse. For simple unmodulated pulse shapes the calculation of the variance is straightforward. For example the variance of the (normalized) Gaussian shaped laser pulse is

$$\sigma^2 = \frac{\Delta t^2}{8 \ln 2}. \tag{25}$$

This relation between the variance and the pulse duration will also be applied as a definition for the pulse duration from the variance of a modulated pulse

$$\Delta t_{\text{mod}} = \sigma_{\text{mod}} \sqrt{8 \ln 2}. \tag{26}$$

However, the analytic expression of the time profile of phase modulated pulses may be overly complicated or even unknown precluding the analytic calculation of the variance. In this case numerical techniques can be used to determine the pulse duration. It is more insightful to calculate the variance directly in the

spectral domain only by referring to the spectral phase function $\varphi(\omega)$. To this end, we assume the shape function of the modulated pulse to be generated by spectral phase modulation in analogy to Equation (16)

$$\tilde{F}_{mod}(\omega) = \tilde{F}(\omega)e^{-i\varphi(\omega)}. \tag{27}$$

If we further assume that the spectrum of the unmodulated function $f(t)$ is real-valued, i.e. it has no additional temporal phase, and the first moment of the unmodulated function vanishes (which is always the case for an even unmodulated shape function $f(t)$ and could be achieved by time-shifting of the unmodulated pulse otherwise), we obtain a convenient expression for the variance of the modulated pulse in the frequency domain

$$\sigma_{mod}^2 = \sigma^2 + \frac{1}{2\pi}\int_{-\infty}^{\infty}[\tilde{F}(\omega)]^2\,[\varphi'(\omega)]^2\,d\omega - \left\{\frac{1}{2\pi}\int_{-\infty}^{\infty}[\tilde{F}(\omega)]^2\,\varphi'(\omega)\,d\omega\right\}^2 \tag{28}$$

where σ^2 denotes the variance of the unmodulated pulse (see for example [41,42] for a derivation). Equation (28) illustrates that the group delay function $\varphi'(\omega)$ determines the pulse duration and provides a powerful tool to calculate the statistical pulse duration even in cases where the pulse shape function is unknown.

2.1.5. Examples of spectral phase functions

We now consider some examples of spectral phase modulation (GDD, TOD, sinusoidal modulation and combinations thereof) which are relevant to the experiments on control of electron dynamics with shaped femtosecond laser pulses presented in this chapter.

2.1.5.1. Polynomial spectral phase modulation functions

A simple approach to understand the physical significance of a spectral phase function $\varphi(\omega)$ with respect to the temporal pulse shape is based on its Taylor series resulting in a sum of polynomial phase functions

$$\varphi(\omega) = \phi_0 + \phi_1 \cdot \omega + \frac{\phi_2}{2!} \cdot \omega^2 + \frac{\phi_3}{3!} \cdot \omega^3 + \cdots \quad . \tag{29}$$

The absolute phase, which relates the carrier oscillation to the envelope, is modulated if the first term ϕ_0 is non-zero. Although this type of modulation can be important for coherent control experiments [43] and

plays an important role for experiments with Carrier-Envelope-Phase (CEP) stabilized femtosecond laser pulses [44-49], it does not influence the pulse envelope and is therefore not considered here. In accordance with the Fourier shift theorem, the linear term in the spectral modulation function $\phi_1 \cdot \omega$ is responsible for a time shift of the pulse envelope by $t = \phi_1$ with respect to the unmodulated pulse. However it should be noted that, unlike the case in interferometric setups, the envelope is shifted rather than a copy of the pulse implying a change of the CEP phase.

Second order spectral phase function

Quadratic phase modulation – also termed Group Delay Dispersion (GDD) – using the spectral phase function

$$\varphi_{GDD}(\omega) = \frac{\phi_2}{2!} \cdot \omega^2 \tag{30}$$

plays a major role in coherent control (see for example [50-56]). Often both the group delay dispersion function

$$GDD(\omega) = \frac{d^2}{d\omega^2} \varphi(\omega) \tag{31}$$

and the modulation parameter ϕ_2 are referred to as GDD. However, only in the special case of polynomial spectral phase modulation up to the second-order both quantities are identical. By applying $\varphi_{GDD}(\omega)$, the modulated spectrum reads

$$\widetilde{\mathcal{E}}_{GDD}(\omega) = \widetilde{\mathcal{E}}(\omega)e^{-i\varphi_{GDD}(\omega)}. \tag{32}$$

As a consequence, the pulse duration of the laser radiation is modified and a linear frequency sweep is introduced. Assuming a bandwidth limited Gaussian input pulse with a pulse duration Δt (see Equation (9)) the chirped pulse remains Gaussian shaped and reads

$$\mathcal{E}_{GDD}(t) = \frac{\mathcal{E}_0}{2} \frac{1}{\gamma^{\frac{1}{4}}} e^{-\frac{t^2}{4\beta\gamma}} e^{i(\alpha t^2 - \epsilon)}, \tag{33}$$

where

$$\alpha = \frac{\phi_2}{8\beta^2\gamma}, \beta = \frac{\Delta t^2}{8\ln 2}, \gamma = 1 + \frac{\phi_2^2}{4\beta^2} \text{ and } \varepsilon = \frac{1}{2}\arctan\left(\frac{\phi_2}{2\beta}\right) \tag{34}$$

featuring an increased variance of

$$\sigma_{GDD}^2 = \sigma^2 + 2\ln(2)\left(\frac{\phi_2}{\Delta t}\right)^2 = \sigma^2 + \delta_{GDD}^2, \tag{35}$$

where δ_{GDD}^2 describes the additional lengthening due to GDD. The frequency sweep is characterized by a linear change of the instantaneous detuning

$$\Delta(t) = 2\,\alpha\,t, \tag{36}$$

where the parameter α

$$\alpha = \left\{ 2\,\phi_2 + \frac{\Delta t^4}{8\,\phi_2[\ln 2]^2} \right\}^{-1} \tag{37}$$

describes the chirp rate. A positive value of ϕ_2 leads to an "up-chirp" characterized by an increase of the instantaneous frequency, whereas a negative ϕ_2 implies a decrease of $\Delta(t)$, known as "down-chirp". With increasing chirp parameter ϕ_2, the pulse duration increases according to Equation (35) accompanied by a reduction in intensity (see Figure 1(a)). Equation (37) shows that the chirp rate is a non-monotonic function of the chirp parameter ϕ_2.

Third order spectral phase function

Third Order Dispersion (TOD) given by the spectral phase function

$$\varphi_{TOD}(\omega) = \frac{\phi_3}{3!} \cdot \omega^3 \tag{38}$$

results in an asymmetric pulse shape and is analytically described by a damped Airy function [30,57]. The analytic expression for the temporal profile reads

$$\mathcal{E}_{TOD}(t) = \frac{\mathcal{E}_0}{2}\sqrt{\frac{\pi}{2\ln 2}}\frac{\Delta t}{|\vartheta|}\,e^{\frac{\ln 2}{2}\frac{\frac{2}{3}\tau - t}{\tau_{1/2}}}\,Ai\left(\frac{\tau - t}{\vartheta}\right) \tag{39}$$

with $\vartheta = \sqrt[3]{\frac{|\phi_3|}{2}}\,\text{sign}(\phi_3)$, $\tau = \frac{\Delta t^4}{32\,\phi_3\,(\ln 2)^2}$ and $\tau_{1/2} = \frac{2\,\phi_3(\ln 2)^2}{\Delta t^2}$, $\tag{40}$

where $Ai(z)$ is the Airy function and the substitutions for ϑ, τ and $\tau_{1/2}$ are so chosen as to describe meaningful physically quantities in units of time. Equation (39) shows that the modulated temporal pulse shape $\mathcal{E}_{TOD}(t)$ is given by the product of an exponentially decaying function with a half-life period of $\tau_{1/2}$ and the Airy function shifted by a delay of τ and scaled by ϑ. Figure 1 (b) shows an example of a pulse subjected to third order dispersion. TOD leads to a quadratic group delay $\varphi'(\omega) = \frac{\phi_3}{2}\omega^2$.

Therefore, for a positive value of ϕ_3, the central frequency of the pulse arrives first, while frequency bands on either side of the central frequency arrive later. The two frequency bands which are symmetrically detuned cause beats in the temporal intensity profile explaining the oscillations after (or before if $\phi_3 < 0$) the main pulse. The beating is also responsible for the phase jumps of π which occur at the zeros of the Airy function. Most of the relevant properties of TOD modulation are determined by the parameter ϑ which is proportional to $\sqrt[3]{|\phi_3|}$. The ratio of $\vartheta/\Delta t$ determines whether the pulse is significantly modulated. As a rule of thumb, only if $|\vartheta/\Delta t| \gg 1$ a series of sub-pulses and phase jumps are observed. Also, the time shift of the most intense sub-pulse with respect to the unmodulated pulse and the FWHM of the sub-pulses are in the order of ϑ. The highly asymmetric TOD pulse is a good example to see that the FWHM is not a representative quantity. Instead, the statistical definition of the pulse duration (Equation (28)) yields a formula similar to Equation (35) for the chirp to describe the duration of the TOD modulated pulse

$$\sigma_{TOD}^2 = \sigma^2 + 2\,[\ln(2)]^2 \left(\frac{\phi_3}{\Delta t^2}\right)^2 = \sigma^2 + \delta_{TOD}^2 \ . \qquad (41)$$

For the applications in materials processing (see Section 4) the remarkable features of TOD are (i) temporal symmetry-breaking of the envelope implying control on the time-dependent energy flux onto the sample and (ii) the ability to produce a short intense pulse accompanied by a weak long pulse train. It has been demonstrated that this type of modulation is well suited to control basic ionization processes to manipulate the ablation dynamics [20,58,59].
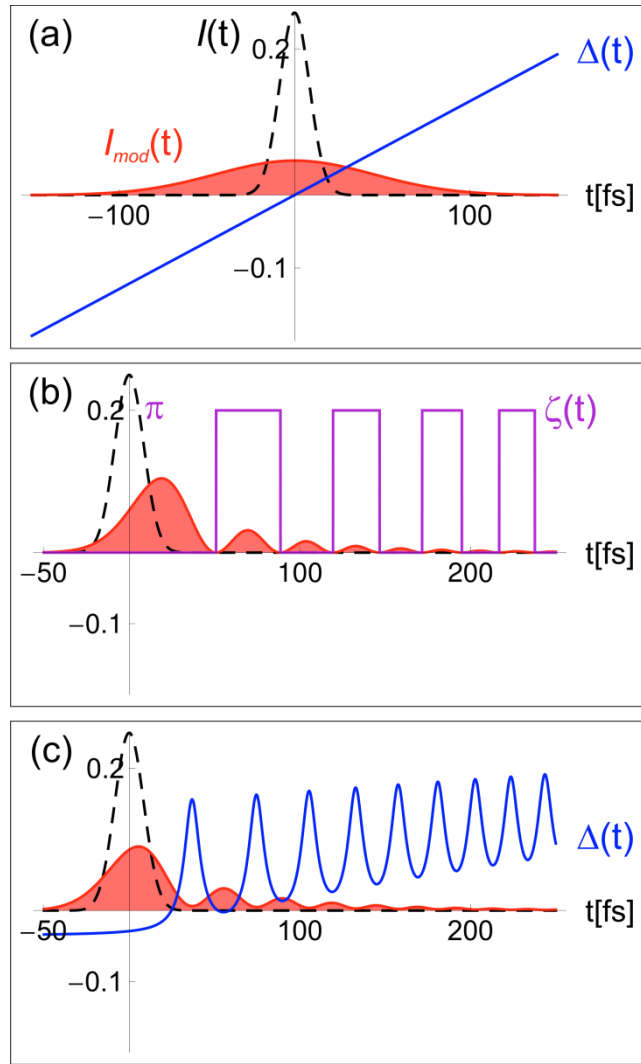
Figure 1 Examples of a spectrally modulated 20 fs (intensity FWHM) pulse. For reference the intensity envelope $I(t)$ of the unmodulated pulse is depicted as black dashed line. The intensity profile $I_{mod}(t)$ of the modulated pulse is shown in red. The blue line indicates the instantaneous detuning $\Delta(t) = \frac{d}{dt}\zeta(t) = \omega(t) - \omega_0$. (a) The second order spectral phase function $\varphi_{GDD}(\omega) = \frac{\phi_2}{2!}\omega^2$ with $\phi_2 = 750$ fs^2 generates a chirped laser pulse with a temporally symmetric intensity distribution and linearly increasing instantaneous frequency. (b) Third Order Dispersion (TOD) $\varphi_{TOD}(\omega) = \frac{\phi_3}{3!}\omega^3$ with $\phi_3 = 20\,000$ fs^3 generates an asymmetric temporal intensity profile at the central frequency, i.e. $\Delta(t) \equiv 0$. Therefore, the temporal phase $\zeta(t)$ is plotted (magenta) rather than the instantaneous frequency. (c) Combination of both spectral modulation functions $\varphi(\omega) = \varphi_{GDD}(\omega) + \varphi_{TOD}(\omega)$ produces an asymmetric intenstity profile with asymmetric instantaneous frequency evolution.

Combined second and third order modulation

An example for the application of combined GDD and TOD modulation along with a derivation of the analytical expression for the field envelope $\mathcal{E}_{GDDTOD}(t)$ can be found in [32]. Here we report the result of the derivation

$$\mathcal{E}_{GDDTOD}(t) = \frac{\mathcal{E}_0}{2} \frac{\Delta t}{|\vartheta|} \sqrt{\frac{\pi}{2 \ln 2}} \; e^{\frac{8}{3\Omega^6 \phi_3^2} - \frac{2\,t}{\Omega^2\,\phi_3}} Ai\left(\frac{\frac{2}{\Omega^4\,\phi_3} - t}{\vartheta} \right) \tag{42}$$

with $\dfrac{1}{\Omega^2} = \dfrac{\ln 4}{\Delta\omega^2} + i \dfrac{\phi_2}{2}$ $\qquad\qquad$ (43)

and ϑ defined in Equation (40). Equation (42) shows that the GDD/TOD-modulated field is again a product of an exponential function and an Airy function. However, since Ω is complex valued both the exponential function and the Airy function have in general complex valued arguments. If $\phi_2 \to 0$, i.e. in the case of pure TOD modulation, the modulated field converges to the exponentially damped Airy function described above. Likewise, the chirped pulse is reproduced if $\phi_3 \to 0$. Combined modulation by GDD and TOD results in complicated pulse shapes with an asymmetric temporal intensity profile as well as a temporally asymmetric instantaneous detuning (see Figure 1 (c)). Coherent control by combined GDD and TOD spectral modulation was reported in a study on the enhancement of the three-photon absorption probability of iodine [60]. More recently, GDD/TOD modulation was used to exert efficient and robust strong-field control on the population transfer in a sensitizer dye [32]. In addition, coherent control of the fluorescence of colloidal semiconductor nanocrystals with combined GDD and TOD modulation has recently been reported [61]. In that publication, it was demonstrated experimentally that GDD/TOD modulated pulses are a versatile spectroscopic tool to probe and to control multi-photon processes. The analytical analysis of the higher-order spectrum reported in [61] revealed that combined GDD and TOD modulation allows to scan the second-order spectrum with a preselected narrow bandwidth by varying ϕ_2 at a given value of ϕ_3. Despite the complicated pulse structure, the pulse duration - calculated in frequency domain by Equation (28) – is obtained by

summation over the contributing additional terms of GDD and TOD suggesting that GDD and TOD modulation are somehow "independent"

$$\sigma_{GDDTOD}^2 = \sigma^2 + 2\ln(2)\left(\frac{\phi_2}{\Delta t}\right)^2 + 2\left[\ln(2)\right]^2\left(\frac{\phi_3}{\Delta t^2}\right)^2 = \sigma^2 + \delta_{GDD}^2 + \delta_{TOD}^2.$$

(44)

2.1.5.2. Periodic spectral phase modulation

Periodic spectral phase modulation functions play an important role in coherent control. Numerous experiments and theoretical studies on coherent control by sinusoidal phase modulation have been carried out on atoms [38,39,43,62,63] and molecules [16,17,64-72]. Applying sinusoidal phase modulation

$$\varphi_{SIN}(\omega) = A\sin(\omega T + \phi) \tag{45}$$

to the spectrum generates the modulated field envelope

$$\mathcal{E}_{SIN}(t) = \sum_{n=-\infty}^{\infty} J_n(A)\,\mathcal{E}(t - nT)\,e^{-in\phi}, \tag{46}$$

where $\mathcal{E}(t)$ is the unmodulated field envelope, and J_n the Bessel function of the first kind and order n. Equation (46) shows that sinusoidal phase modulation in frequency domain produces a sequence of sub-pulses with a temporal separation determined by the parameter T and well defined relative temporal phases controlled by the absolute phase ϕ of the sine function. Provided the individual sub-pulses are temporally separated, i.e. $T \gg \Delta t$, the envelope of each sub-pulse is a scaled and shifted replica of the unmodulated pulse envelope. The amplitudes of the sub-pulses are controlled by the modulation parameter A via the Bessel function $J_n(A)$. If the temporal separation of the pulses is smaller than the pulse duration, i.e. $T \ll \Delta t$, the sub-pulses with different phases overlap giving rise to a complicated temporal profile and variations of the instantaneous frequency (see Figure 2(c)). A more detailed description of the effect of sinusoidal phase modulation can be found in [39,63]. Experiments on coherent control of ultrafast electron dynamics by intense sinusoidally modulated fields will be discussed in Section 3.3.4 and 3.3.5.
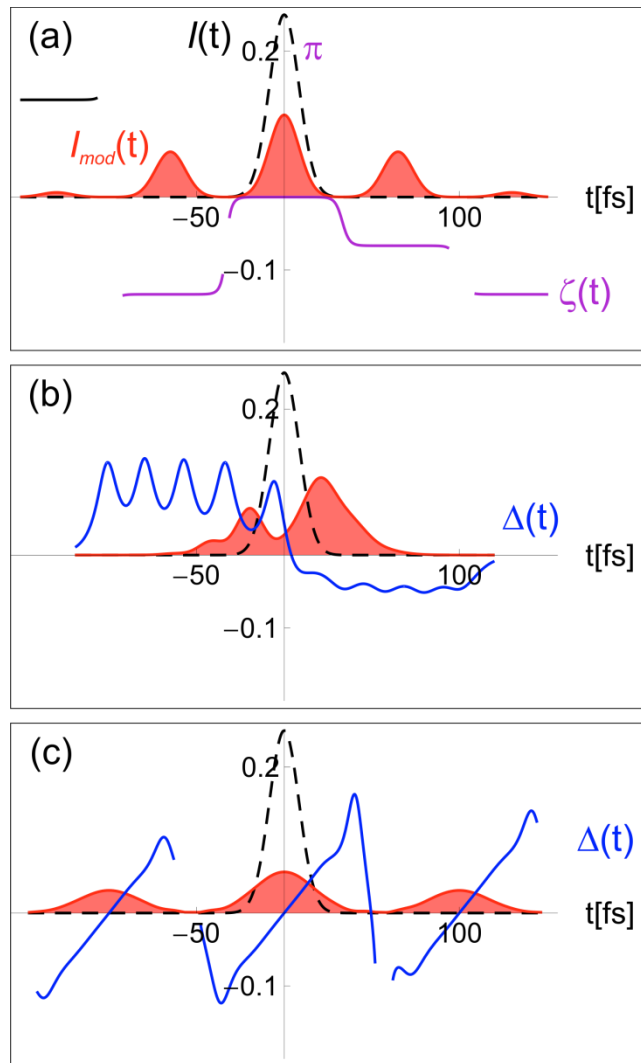
Figure 2 Sinusoidal spectral phase modulation $\varphi_{SIN}(\omega) = A \sin(\omega T + \phi)$ produces pulse sequences with phase jumps between adjacent sub-pulses. (a) sinusoidal phase modulation with the parameters $A = 1.2, T = 65$ fs and $\phi = \pi/3$ leading to a sequence of separated pulses. Note that in (a) the temporal phase $\zeta(t)$ is plotted (magenta) rather than the instantaneous frequency. (b) sinusoidal modulation with the parameters $A = 2.0, T = 20$ fs and $\phi = \pi/3$ leads to overlapping sub-pulses. (c) Combination of sinusoidal and GDD modulation with the parameters $A = 1.2, T = 100$ fs, $\phi = \pi/4$ and $\phi_2 = 250$ fs^2. This combination generates a sequence of chirped pulses. The frequency sweep of each sub-pulse is seen in the instantaneous detuning $\Delta(t)$.

2.1.6. Polarization shaping

A new degree of control became accessible with the ability to control the time-dependent polarization state of a femtosecond laser pulse in addition to its temporal structure [73]. The physical rational for the enhanced controllability is

the manipulation of the vectorial properties of the light-matter interaction. Polarization shaping was for instance applied to coherent control of atomic and molecular dynamics [74-77], adaptive sub-wavelength control of nano-optical fields [78] and non-linear microscopy [79]. In addition, polarization-shaped laser pulses have been used to create polarization-shaped ultraviolet femtosecond pulses [80] and double pulse sequences with zeptosecond precision [35]. In general, any polarization state can be created by the superposition of two orthogonal linearly polarized fields with appropriate phases. Therefore, in order to describe polarization-shaped pulses, we start by considering the time-dependent unmodulated field envelope perpendicular to the propagation direction

$$\vec{\mathcal{E}}(t) = \begin{pmatrix} \mathcal{E}_x(t) \\ \mathcal{E}_y(t) \end{pmatrix}.$$
(47)

Independent spectral phase modulation of two orthogonal components of the spectrum $\vec{\widetilde{\mathcal{E}}}(\omega) = \left(\widetilde{\mathcal{E}}_x(\omega), \widetilde{\mathcal{E}}_y(\omega) \right)$ by the two phase functions $\varphi_x(\omega)$ and $\varphi_y(\omega)$ using

$$\begin{pmatrix} \widetilde{\mathcal{E}}_{x,mod}(\omega) \\ \widetilde{\mathcal{E}}_{y,mod}(\omega) \end{pmatrix} = \begin{pmatrix} \widetilde{\mathcal{E}}_x(\omega) \, e^{-i\varphi_x(\omega)} \\ \widetilde{\mathcal{E}}_y(\omega) \, e^{-i\varphi_y(\omega)} \end{pmatrix}$$
(48)

yields two linearly polarized modulated spectral light fields $\widetilde{\mathcal{E}}_{x,mod}(\omega)$ and $\widetilde{\mathcal{E}}_{y,mod}(\omega)$ resulting in the polarization-shaped temporal field

$$\vec{\mathcal{E}}_{mod}(t) = \begin{pmatrix} \mathcal{E}_{x,mod}(t) \\ \mathcal{E}_{y,mod}(t) \end{pmatrix},$$
(49)

where the complex valued temporal envelope functions $\mathcal{E}_{x,mod}(t)$ and $\mathcal{E}_{y,mod}(t)$ are obtained by inverse Fourier transform of the respective modulated spectra [76]. Although both components of the time dependent envelope of the modulated field $\mathcal{E}_{x,mod}(t)$ and $\mathcal{E}_{y,mod}(t)$ fully describe the polarization-shaped femtosecond laser pulse, we introduce the instantaneous polarization state and the instantaneous frequency in order to better characterize its physical properties [73]. For a simplified notation we will momentarily suppress the index *mod* in Equation (49) and use instead Equation (47) to describe the modulated field as well. Similar to the linearly polarized case (Equation (5)), the real valued fast oscillating field is obtained by

$$\vec{E}(t) = \begin{pmatrix} E_x(t) \\ E_y(t) \end{pmatrix} = Re[\vec{\mathcal{E}}(t) \, e^{i\,\omega_0\,t}] = Re\left[\begin{pmatrix} \mathcal{E}_x(t) \\ \mathcal{E}_y(t) \end{pmatrix} e^{i\,\omega_0\,t}\right]. \tag{50}$$

Instantaneous ellipticity

In order to characterize the instantaneous polarization state, we derive the parameters to define the instantaneous ellipticity. To this end, the slowly varying envelope function $\vec{\mathcal{E}}(t)$ is assumed to be constant over one optical period, thus the ellipticity within this time interval is well-defined. In order to determine the ellipticity parameters at a given time t_0 within the pulse, we start by considering the initial electric field amplitudes $A = |\mathcal{E}_x(t_0)|$ and $B = |\mathcal{E}_y(t_0)|$ with the respective temporal phases $\alpha = \mathrm{Arg}[\mathcal{E}_x(t_0)]$ and $\beta = \mathrm{Arg}[\mathcal{E}_y(t_0)]$. The ellipse is constructed by multiplication of the initial complex valued electric field vector

$$\vec{\mathcal{E}}(t_0) = \begin{pmatrix} \mathcal{E}_x(t_0) \\ \mathcal{E}_y(t_0) \end{pmatrix} = \begin{pmatrix} A\,e^{i\,\alpha} \\ B\,e^{i\,\beta} \end{pmatrix} \tag{51}$$

with the phase factor $e^{i\,\chi}$, where χ sweeps through the interval of $(0,2\pi)$. Accordingly, the real valued field reads

$$\vec{E}(\chi) = \begin{pmatrix} E_x(\chi) \\ E_y(\chi) \end{pmatrix} = Re\left[\begin{pmatrix} \mathcal{E}_x \\ \mathcal{E}_y \end{pmatrix} e^{i\,\chi}\right] = Re\left[\begin{pmatrix} Ae^{i\,\alpha} \\ Be^{i\,\beta} \end{pmatrix} e^{i\,\chi}\right] = \begin{pmatrix} A\,\cos(\chi + \alpha) \\ B\,\cos(\chi + \beta) \end{pmatrix} \tag{52}$$

and hence $\vec{E}(\chi)$ describes an ellipse around the origin (see Figure 3). If $\alpha = \beta \pm n\pi$, the ellipse degenerates yielding linearly polarized light. Initially, the angle of the electric field vector $\vec{E}(0)$ is described by

$$\varepsilon_0 = \arctan\left(\frac{B\,\cos(\beta)}{A\,\cos(\alpha)}\right). \tag{53}$$

The phases χ_1 and χ_2 of the two semi axes relative to the initial phases α and β are given by

$$\chi_1 = \frac{1}{4i}\ln(z) \text{ and } \chi_2 = \chi_1 + \frac{\pi}{2}, \text{ with } \quad z = \frac{A^2 e^{-2i\alpha} + B^2 e^{-2i\beta}}{A^2 e^{2i\alpha} + B^2 e^{2i\beta}} \tag{54}$$

being a complex number with the modulus of unity, i.e. $|z| = 1$. Therefore, the phases χ_1 and χ_2 are both real valued. Because $\chi_2 = \chi_1 + \frac{\pi}{2}$, it is sufficient to specify one of the two phases. The angle of both semi axes of the polarization ellipse is determined by adding the phases χ_1 and χ_2 to the initial phases α and β respectively, i.e. $\alpha + \chi_1$ and $\beta + \chi_1$ for one semi axis and $\alpha + \chi_2$ and $\beta + \chi_2$ for the other. The angles of both axes read explicitly

$$\varepsilon_a = \arctan\left(\frac{B \, \cos(\beta+\chi_1)}{A \, \cos(\alpha+\chi_1)}\right) \text{ and } \varepsilon_b = \arctan\left(\frac{B \, \cos(\beta+\chi_2)}{A \, \cos(\alpha+\chi_2)}\right). \tag{55}$$

The modulus of the vector $\vec{E}(\chi)$ describing the ellipse reads

$$\left|\vec{E}(\chi)\right| = \sqrt{E_x^2(\chi) + E_y^2(\chi)} = \sqrt{A^2\cos^2(\chi + \alpha) + B^2\cos^2(\chi + \beta)}. \tag{56}$$
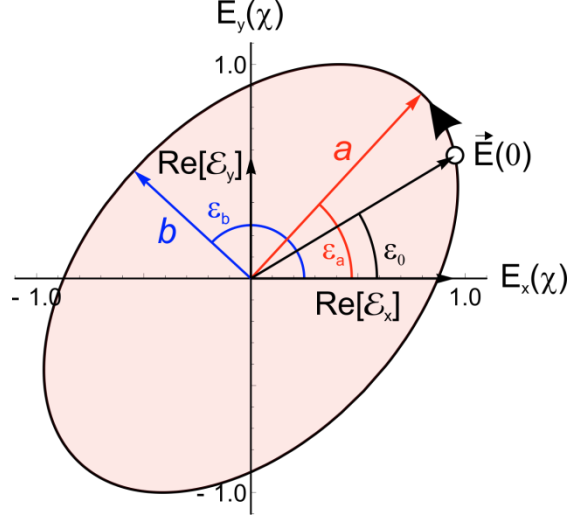

Figure 3 Instantaneous polarization ellipse for one optical cycle. The ellipse is generated by the electric field vector $\vec{E}(\chi)$, where χ sweeps through the interval of $(0,2\pi)$. Initially, the electric field vector starts at the position $\left(Re[\mathcal{E}_x], Re[\mathcal{E}_y]\right)$ with an angle ε_0 and evolves in the direction of the large arrow on the ellipse. The instantaneous polarization state is characterized by the semi axes a and b and one of the corresponding angles ε_a and ε_b.

A convenient way to derive the relative phases χ_1 and χ_2 of the two semi axes is based on determining the extreme values of the modulus of the field as a function of the phase χ. Equipped with the two relative phases of the extreme values, the length of the two semi axes is calculated by

$$a = \left|\vec{E}(\chi_1)\right| = \sqrt{E_x^2(\chi_1) + E_y^2(\chi_1)} \text{ and}$$

$$b = \left|\vec{E}(\chi_2)\right| = \sqrt{E_x^2(\chi_2) + E_y^2(\chi_2)}. \tag{57}$$

The instantaneous polarization state is defined by the two semi axes a and b along with the respective rotation angles of the ellipse ε_a and ε_b. Since the two semi axes of the ellipse are at right angle, one of the angles ε_a and ε_b is sufficient for the construction of the ellipse. Note that the mapping of a and b to the major and minor semi axis is not unique. However, the mapping is directly related to the initial field parameters by

$$c = a^2 - b^2 = A^2 \, Re[z \, e^{2i\alpha}] + B^2 \, Re[z \, e^{2i\beta}]. \tag{58}$$

If $c > 0$, then a is the major semi axes, otherwise, if $c < 0$, b is the major axis. The instantaneous polarization is circular if $c = 0$. In all figures showing polarization-shaped pulses, the ellipses with the two semi axes a and b rotated by the corresponding angle were used to represent the instantaneous ellipticity for the shaped pulses. The color coding for the ellipses is derived from the instantaneous frequency.

The above analysis yields explicit values for both semi-axes and the corresponding rotation angle. Alternatively, the vectors of both semi axes $\vec{a}$ and $\vec{b}$ can be derived employing *singular value decomposition* (SVD) of a matrix $\mathcal{M}$, which represents the ellipse defined in Equation (52):

$$\vec{E}(\chi) = \begin{pmatrix} A \ \cos(\chi + \alpha) \\ B \ \cos(\chi + \beta) \end{pmatrix}.$$

Starting from the above representation we define the vectors

$$\vec{A} = \begin{pmatrix} A \ \cos(\alpha) \\ B \ \cos(\beta) \end{pmatrix} \tag{59a}$$

and

$$\vec{B} = \begin{pmatrix} A \ \sin(\alpha) \\ B \ \sin(\beta) \end{pmatrix} \tag{59b}$$

so as to obtain

$$\vec{E}(\chi) = \vec{A} \cos(\chi) - \vec{B} \sin(\chi) = \mathcal{M} \begin{pmatrix} \cos(\chi) \\ \sin(\chi) \end{pmatrix} \tag{60}$$

with the matrix

$$\mathcal{M} = \begin{pmatrix} A \ \cos(\alpha) & -A \ \sin(\alpha) \\ B \ \cos(\beta) & -B \ \sin(\beta) \end{pmatrix}. \tag{61}$$

Through SVD, the matrix $\mathcal{M}$ is decomposed into

$$\mathcal{M} = \mathcal{T} \Lambda \mathcal{S}^{\dagger} \tag{62}$$

where $\mathcal{T}$ and $\mathcal{S}^{\dagger}$ are unitary rotation matrices and Λ is a diagonal matrix containing the singular values of $\mathcal{M}$. The two semi axes $\vec{a}$ and $\vec{b}$ are then obtained by

$$\vec{a} = \mathcal{T} \Lambda \vec{e}_1 \tag{63a}$$

$$\vec{b} = \mathcal{T} \Lambda \vec{e}_2. \tag{63b}$$

Instantaneous frequency

In order to provide a unique color for each ellipse, we determine a single time dependent instantaneous frequency $\varpi(t)$ for the polarization-shaped pulse which is in general composed of two components with different time dependent instantaneous frequencies $\omega_x(t)$ and $\omega_y(t)$. We strive to obtain an expression for the instantaneous frequency which is derived without ambiguities from inverse trigonometric functions and which is physically plausible. To this end, we need to slightly generalize the ansatz made in Equation (52) by writing

$$\vec{E}(t) = \begin{pmatrix} E_x(t) \\ E_y(t) \end{pmatrix} = Re\left[\begin{pmatrix} \mathcal{E}_x(t)\, e^{i\,\omega_x\, t} \\ \mathcal{E}_y(t)\, e^{i\,\omega_y\, t} \end{pmatrix} \right] \tag{64}$$

in order to allow for two different frequencies ω_x and ω_y. Here, we assume that the two frequencies ω_x and ω_y are time independent over one optical cycle and have already been determined from the complex fields, for example with the help of Equation (6). By evaluating the real part in Equation (64) and again assuming that A, B, α and β are constant over one optical period, we see that

$$\vec{E}(t) = \begin{pmatrix} A\, \cos(\omega_x\, t + \alpha) \\ B\, \cos(\omega_y\, t + \beta) \end{pmatrix} \tag{65}$$

and hence, we obtain for the modulus of $\vec{E}(t)$ similar to Equation (56)

$$\left| \vec{E}(t) \right| = \sqrt{E_x^2(t) + E_y^2(t)} = \sqrt{A^2\, \cos^2(\omega_x\, t + \alpha) + B^2\, \cos^2(\omega_y\, t + \beta)}. \tag{66}$$

During one optical cycle the electric field vector sweeps twice through the apex giving rise to two maxima. Therefore, the time dependent modulus of the electric field oscillates with double the instantaneous frequency (see Figure 4). The instantaneous frequency is determined by applying again Equation (6) to the analytic signal corresponding to $\left| \vec{E}(t) \right|^2$

$$\frac{1}{4}A^2 e^{2i(\omega_x\, t + \alpha)} + \frac{1}{4}B^2 e^{2i(\omega_y\, t + \beta)} \tag{67}$$

and subsequent division by two. Ignoring the oscillatory terms, we obtain

$$\varpi(t) = \frac{A^4\, \omega_x(t) + B^4\, \omega_y(t)}{A^4 + B^4}, \tag{68}$$

i.e. the instantaneous frequency of the polarization-shaped laser pulse $\varpi(t)$ is the weighted average of the instantaneous frequencies $\omega_x(t)$ and $\omega_y(t)$ of the two electric field components where the weights are determined by the field

amplitudes A^4 and B^4. Equation (68) displays the physically expected properties for the limiting values, for example $\varpi = \omega_x = \omega_y$ if both instantaneous frequencies are equal. If one component vanishes (say $B = 0$) the frequency is determined by the other component $\varpi = \omega_x$ and if both field components have the same amplitude $A = B$, the frequency is the arithmetic mean $\varpi = \frac{\omega_x + \omega_y}{2}$ of both frequencies.
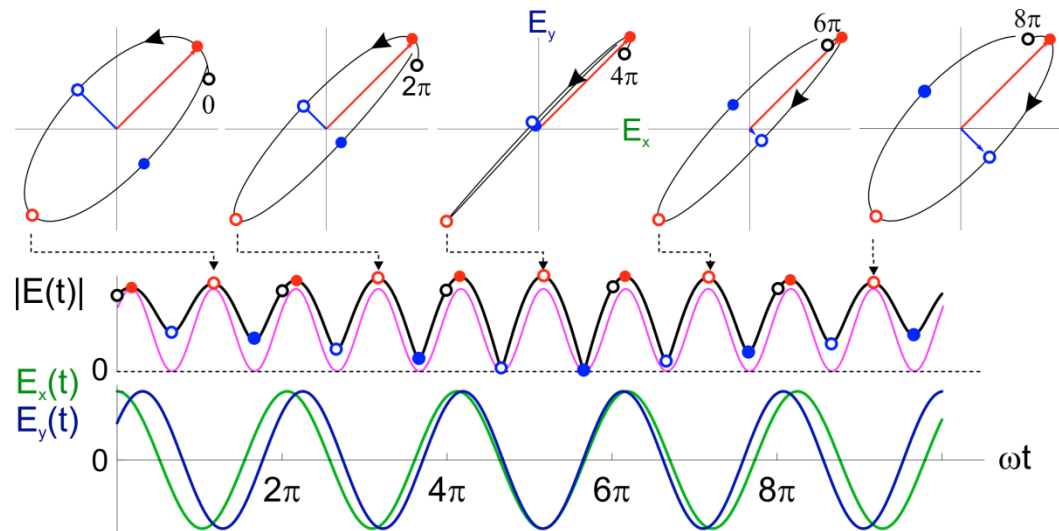

Figure 4 The field $\vec{E}(t)$ (upper panels) with the two components $E_x(t)$ and $E_y(t)$ (lower panel) with different instantaneous frequencies ω_x and ω_y describes only approximate ellipses. The comparison between the oscillations of $|\vec{E}(t)|$ (thick black line) and the sinusoidal oscillation with a frequency of $\varpi(t)$ (middle) shows good agreement. Red dots indicate the positions of the major semi axis whereas the blue dots show the positions of the minor semi axis.

Figure 4 shows the oscillations of $|\vec{E}(t)|$ (thick black line) which are used to define the instantaneous frequency of a polarization-shaped femtosecond laser pulse. For clarity, ω_x and ω_y have been chosen time independent in this illustration. The comparison with the sinusoidal oscillation with the frequency $\varpi(t)$ shows good agreement. Because the field has two different instantaneous frequencies ω_x and ω_y, the field vector $\vec{E}(t)$ describes only approximately an ellipse during one optical cycle, i.e. the ellipses are "open". Due to the difference in frequency the semi axes change their length and orientation. The red dots in Figure 4 indicate the positions of the major semi axis whereas the

blue dots show the positions of the minor semi axis. Note that the field $\left|\vec{E}(t)\right|$ has two maxima and two minima for each oscillation as seen by comparison of $\left|\vec{E}(t)\right|$ with $E_x(t)$ and $E_y(t)$ in Figure 4. Figure 5 shows a gallery of prototypical polarization-shaped laser pulses generated by the above procedure.
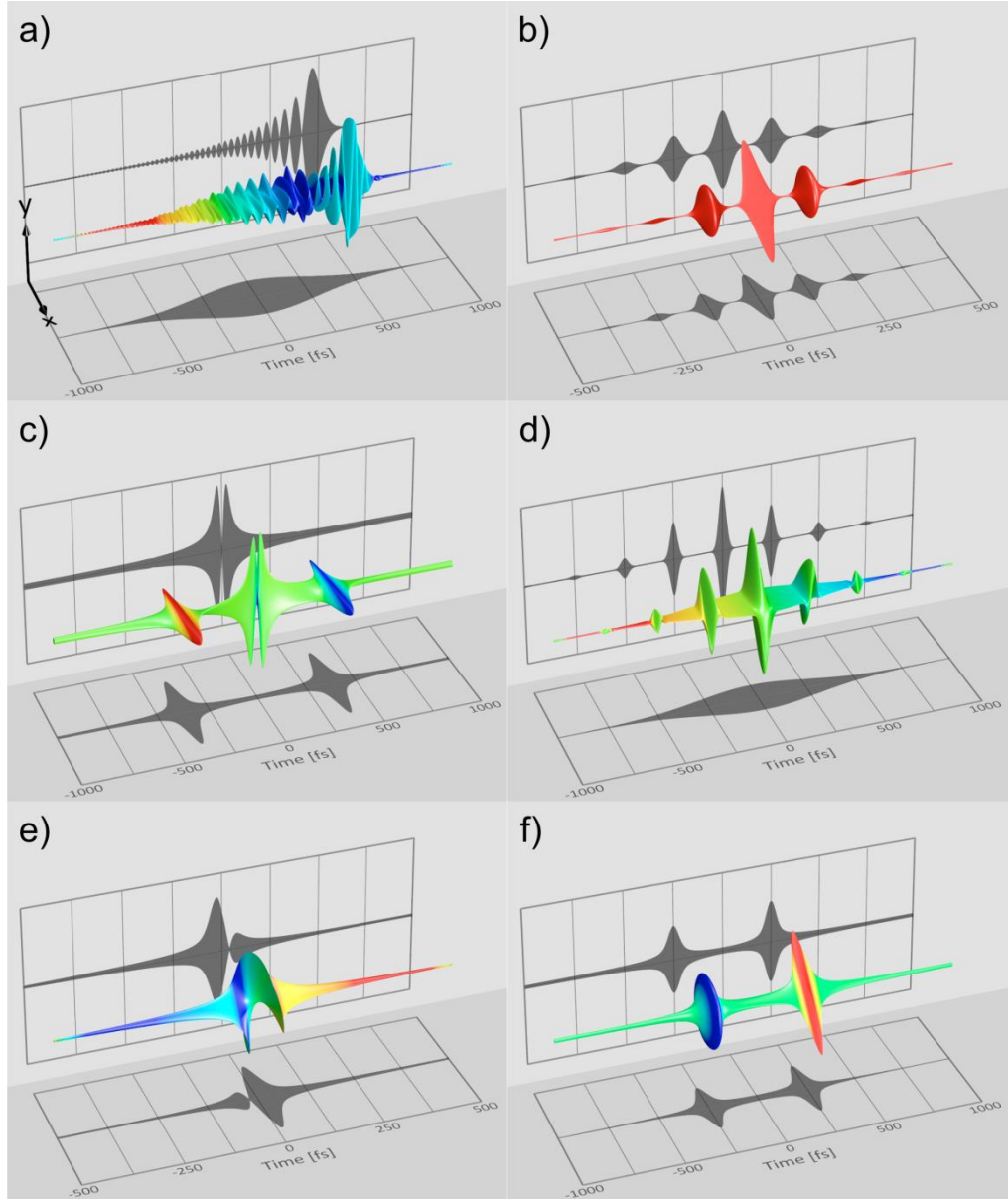

Figure 5 Gallery of polarization-shaped laser pulses represented by ellipses with the semi axes a and b rotated by the respective angles ε_a and ε_b. The color represents the instantaneous frequency according to Equation (68). The spectral phase functions are (a) $\varphi_x(\omega) = \frac{\phi_2}{2!}\omega^2$ and $\varphi_y(\omega) = \phi_1\omega + \frac{\phi_3}{3!}\omega^3$ with $\phi_1 = 500$ fs, $\phi_2 = 5000$ fs² and $\phi_3 = -32000$ fs³, (b) $\varphi_x(\omega) = \sin(\omega T)$ and $\varphi_y(\omega) = \cos(\omega T)$ with $T = 125$ fs, (c) $\varphi_x(\omega) = \tau|\omega|$ and $\varphi_y(\omega) = \frac{\pi}{2}\text{sign}(\omega)$ with $\tau = 375$ fs, (d) $\varphi_x(\omega) = \frac{\phi_2}{2!}\omega^2$ and $\varphi_y(\omega) = \sin(\omega T)$ with $\phi_2 = 5000$ fs² and $T = 250$ fs, (e) $\varphi_x(\omega) = -\frac{1}{4}\arctan\left(\frac{\omega + \delta\omega}{\Delta\omega}\right)$

and $\varphi_y(\omega) = -\frac{\pi}{2} + \frac{1}{4}\arctan\left(\frac{\omega - \delta\omega}{\Delta\omega}\right)$ with $\delta\omega = 1$ mradfs^{-1} and $\Delta\omega = 1.25$ mradfs^{-1},

(f) $\varphi_x(\omega) = \tau|\omega - \delta\omega|$ and $\varphi_y(\omega) = \tau|\omega - \delta\omega| + \frac{\pi}{4}\text{sign}(\omega - \delta\omega)$ with $\tau = -250$ fs

and $\delta\omega = 5$ mradfs^{-1}.

2.2. Experimental implementation

Various experimental laser pulse shaping techniques are reviewed in the literature
[9,30,31,81-83]. Recently, precision pulse shaping down to the zeptosecond regime
has been reported opening the route to control electron dynamics with
unprecedented precision [35]. A spectral phase modulator generating quasi-
arbitrary spectral phase functions $\varphi(\omega)$ can be experimentally implemented
employing a 4*f*-setup (see Figure 6). In the setup shown in Figure 6, the ultrashort
laser pulse is spatially resolved in its spectral components by a grating and imaged
onto a liquid crystal display (LCD) situated in the Fourier plane of the 4*f*-setup. In the
Fourier plane the spectral phase shaping is achieved by space-selective phase
modulation via the LCD. Behind the LCD, the spectral components of the pulse are
merged again by another grating. For highest possible throughput reflective optics
are preferred. Especially the efficiency of gratings in terms of spectrally resolved
reflectivity and/or transmittance of the laser radiation should be uniform over the
laser spectrum. The LCD should feature a high damage threshold for optimal
throughput and a large number of pixels (implying high spectral resolution) allowing
for the production of complex shaped pulses ranging from the femtosecond to
several tens of picoseconds. A design of a compact and robust spectral phase
modulator was presented in [82] and extended towards a polarization shaper with
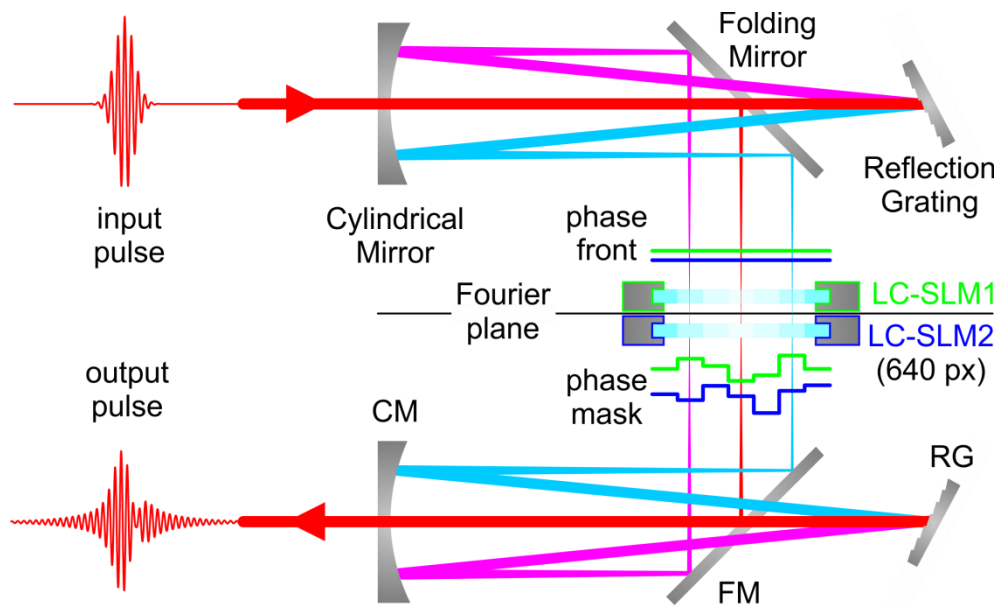reflective optics and transmission gratings [76].

Figure 6 Schematic setup of a compact and robust spectral phase modulator based on a Liquid Crystal Display (LCD) situated in the Fourier plane of a 4f zero dispersion compressor. The incoming laser beam is diffracted and spatially dispersed by the first reflection grating (RG). A Cylindrical Mirror (CM) images the spectral component into the Fourier plane, where each component is individually retarded by the different pixels of the LCD. The group delay which a certain pixel introduces is computer-controlled by the voltage applied to the pixel. The whole setup is built symmetrically with respect to the Fourier-plane, so that a second pair of CM and RG reconstructs the laser beam spatially. Interference of the phase-modulated spectral components in space and time yields a shaped temporal laser pulse at the output of the pulse shaper.

2.3. Adaptive optimization

Modern pulse shaping devices with typically 640 pixels for the modulation of both individual spectral polarization components make available a huge number of laser pulse shapes. Therefore, it is in practice very difficult to find an optimal laser pulse which guides the quantum system most efficiently from the initial state into a preselected final target state. If the relevant physical mechanisms are already identified, optimal light fields can be found by fine tuning the parameters of physically motivated pulse shapes [40,64,69,84-86]. However, if the systems are too complex, adaptive feedback learning loops [87-93] provide a solution to this high dimensional search space problem. Genetic algorithms are often employed to carry out the optimization procedure [87,88,90,91,94]. In this iterative procedure the shape of the laser pulse is described by a set of parameters, similar to the genetic

code of a biologic individual. The fitness, i.e. some measure for the adequacy of the pulse shape with respect to a certain optimization target, is measured in the experiment. Via selection of the best individuals and creation of new pulse shapes being offspring of those best individuals, optimally adapted pulse shapes are found analogous to evolution in biology based on "survival of the fittest". Also other optimization procedures such as the covariance matrix adaption evolutionary strategy (CMA-ES) [95] have been implemented in coherent control [96].

3. **Isolated model systems**.

In the first part of this review we focus on coherent control of Resonance Enhanced Multiphoton Ionization (REMPI) of isolated model systems in the gas phase using shaped femtosecond laser pulses. We discuss the interaction of well-defined shaped pulses with simple prototype systems such as atoms or dimers in order to allow for a detailed analysis of the underlying physical mechanisms by comparison of experimental results with simulations. In addition, on the femtosecond time scale, atoms or molecules in the gas phase are unaffected by perturbations of the environment such as de-coherence processes due to collisions or interactions with a solvent. Because the coherence of matter waves is the prerequisite for coherent control, we begin our analysis by studying the coherence transfer from light to matter waves on isolated model systems. Specifically, we investigate the transfer of the coherence properties of a two pulse sequence to free electron wave packets. Building on this simple example, the physical mechanism of three-dimensional coherent control of free electron wave packets by polarization-shaped laser pulses is investigated in some detail. A novel experimental tool to measure these three-dimensional photoelectron distributions by tomographic reconstruction is introduced and sample results including the measurement of so-called designer electron wave packets are shown. Then, two examples of adaptive optimization of ionization using polarization-shaped femtosecond laser pulses are presented. The first one demonstrates maximization of the ionization yield in potassium dimers whereas in the second example the projection of a designer free electron wave packet is optimized. The last part of this section is devoted to strong-field control of coherent electron dynamics in atoms and the coupled electron-nuclear dynamics in molecules. Intense laser pulses, entailing non-perturbative interactions of the light field with the atoms or

molecules, open new physical mechanisms for efficient coherent control. Prominent strong-field control schemes are presented and discussed with regard to efficient switching of electronic excitation on the ultrafast timescale.

3.1. Coherence transfer from light to matter.

In order to better understand the physical mechanisms of coherent control and, in particular, coherent control of electron dynamics, it is essential to consider the quantum physical wave nature of the electron. In photo-ionization, for example, the wave picture describes the detached electron as a somehow localized free wave packet consisting of the superposition of many plane waves. Their amplitudes are manipulated by controlling the constructive and destructive quantum mechanical interference by coherent light sources such as ultrafast lasers. Therefore, the transfer of the coherence properties of light to matter waves is crucial to controlling ultrafast coherent dynamics of matter waves. Experimentally, coherence transfer from shaped laser pulses to matter waves was demonstrated on the interference of free electron wave packets by the photo-ionization of atoms with a coherent double pulse sequence [97]. Besides this fundamental aspect of photo-ionization with coherent radiation, interferences in the photoelectron spectrum have become an established tool to characterize ultrashort femtosecond and attosecond laser pulses [98-101].

3.1.1. Interference of free electron wave packets

In the experiments on the interference of free electron wave packets photoelectron kinetic energy spectra were measured to probe the coherence properties of the matter waves. To elucidate the physical picture of the creation, propagation and observation of a coherent free electron wave packet we first consider single pulse ionization and subsequently discuss the transfer of the coherence properties in a double pulse scenario.

Single pulse ionization

In the above experiment, potassium atoms have initially been prepared in the excited $5p$ state by using the second harmonic ($2h\upsilon$) of an 800 nm femtosecond

laser pulse in order to study one photon ionization (see energy level scheme in Figure 7 (a)). After the ionization from the excited $5p$ state with the fundamental laser radiation at time T_1, a localized electron wave packet with an average kinetic energy of $E_{kin} = 3h\nu - IP$ is launched from the interaction region, where IP denotes the ionization potential. The calculated time evolution of the wave packet is depicted in Figure 7 (b). Due to the quadratic dispersion relation of matter waves in vacuum $E(k) = \frac{\hbar^2 k^2}{2m}$ the wave packet broadens during its further propagation (T_2 and T_3) - a textbook example of the dispersion of a quantum mechanical matter wave packet (see for example [102,103]). It turns out that the wave packet evolves into its own momentum distribution [22,99] as observed with a TOF (time-of-flight) photoelectron spectrometer.

Double pulse ionization

As depicted in Figure 7 (c) and (d), the ionization with a coherent double pulse illustrates how a structured electron wave packet is created by the interference of the two partial wave packets. Since the alkali metal potassium possesses only a single outer electron, in the weak-field using infrared pulses at most one electron can be detached from a single atom during the light matter interaction. There is a certain probability amplitude for ionization by the first laser pulse and the same probability amplitude during the second pulse. The corresponding double peaked wave packet at the time T_1 is described by the probability density $|\psi(x, t = T_1)|^2$ shown in Figure 7 (d). Due to the aforementioned dispersion of matter waves both partial wave packets spread in space and start to overlap. The interference of both partial wave packets - effectively the interference of the electron with itself- is responsible for the subsequent transient interference pattern shown at T_2. At some later time (T_3) a quasi stationary wave packet appears which still broadens in space but does not change its qualitative shape. Again, the wave packet evolves into its momentum distribution which consists of a series of equidistant interference fringes. Those interferences observed in the photoelectron time-of-flight spectrum reveal the transfer of coherence in the double pulse sequence to the electron waves.
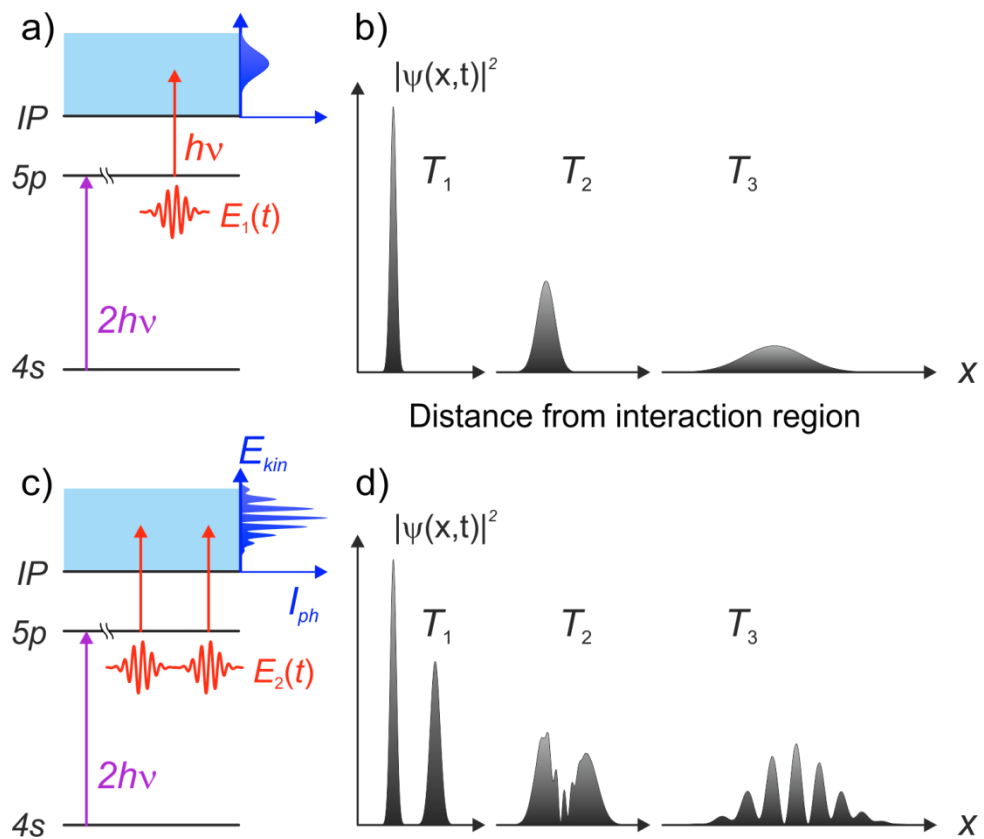
Figure 7 In order to study the coherence transfer from light to matter waves in single photon ionization the initial $5p$ state is prepared by excitation with the second harmonic ($2h\nu$) of an infrared femtosecond laser pulse. (a) Level scheme for the ionization from the potassium $5p$ excited state with a single femtosecond laser pulse ($E_1(t)$ red) leads to a broad spectrum of photo electron kinetic energies $E_{kin} = 3h\nu - IP$ (blue photoelectron spectra above the ionization potential IP). (b) During the time evolution the wave packet broadens in coordinate space as shown for the subsequent time steps $T_1 < T_2 < T_3$. (c) Ionization scheme for double pulse ionization. (d) Due to the coherent light matter interaction, the ionization by a coherent double pulse ($E_2(t)$) leads to an interference of the two coherent matter waves in the continuum. At T_1 both electron wave packets are separated whereas transient interference structures appear at T_2. The long term evolution ($t > T_3$) gives rise to a stationary interference pattern that is observed in the photoelectron spectrum.

3.1.2. Analogy to the double slit experiment

The analogy of the interfering matter waves in coherent control to the interference of classical waves in the celebrated Young's double slit experiment has been pointed out already in the early days of coherent control by Brumer

and Shapiro [104]. The close analogy of the two interfering free electron wave packets demonstrated in the above experiment to the Young's double-slit experiment is particularly enlightening. In this spirit, the interference of the free electron wave packets is regarded as a "Young's double-slit in the time domain" [97,98] because the visibility of the interference pattern is complementary to the "which way information" on the photo-ionization process, i.e. the information whether the ionization took place during the first or the second laser pulse. By analyzing the interaction of an intense two pulse sequence in the dressed states basis (see also Section 3.3. for a discussion of the dressed states), the double slit analogy was extended to strong field ionization [105].

3.2. Control by polarization-shaped laser pulses

By controlling the vectorial properties of the light-matter interaction, polarization shaping gives access to the three-dimensional temporal response of atomic and molecular systems [75]. In this section we start by discussing the physical mechanism of the creation of shaped free electron wave packets by multiphoton ionization with elliptically polarized pulses. This example serves as a prototype for three-dimensional control with polarization-shaped laser pulses [22,106] which is described in a subsequent section.

3.2.1. Physical mechanisms

In the double pulse experiment, the momentum distribution was shaped by the interference of the two ionization pathways provided by the two pulses [97,99]. In general, much more versatile manipulation of a quantum system may be attained by controlling the interference of multiple quantum pathways. In order to illustrate the interference of multiple quantum pathways, we consider the 1+2 REMPI of potassium atoms with polarization-shaped 800 nm femtosecond laser pulses. For the analysis, we decompose the REMPI process into an initial step, i.e. control of the amplitudes of superposition states during the interaction via multiple quantum pathways with a time-dependent ellipticity of the pulse (see Section 2.1.6 on polarization shaping), and the subsequent interference of multiple partial waves during their propagation in the continuum.

Polarization control of multiple pathways

We start by considering the bound and free quantum states characterized by the angular momentum quantum numbers $l = 0, 1, 2, 3 = s, p, d, f$ and $m = -l, .., l$ ignoring the spin for simplicity [76,107]. For the absorption of the three required light quanta in a 1+2 REMPI process, three different l-quantum pathways (ladders) are allowed due to the Δl selection rules, i.e. $s \rightarrow p \rightarrow d \rightarrow f$, $s \rightarrow p \rightarrow d \rightarrow p$ and $s \rightarrow p \rightarrow s \rightarrow p$ (see Figure 8). As a consequence, the final continuum states consist of superposition states with f and p character. In multiphoton ionization with linearly polarized laser pulses the $\Delta m = 0$ selection rule applies in addition and therefore the initial $m = 0$ state is exclusively connected with final $m = 0$ states (not shown). In contrast, multiphoton ionization using elliptically polarized light – being a superposition of left and right handed circularly polarized light fields entailing the selection rules $\Delta m = \pm 1$ - creates superposition states in the continuum with different values of m. For example, three photon ionization of potassium atoms with elliptically polarized light creates superposition states consisting of four f states with $m = -3, -1, 1, 3$ and two p states with $m = -1, 1$ (see Figure 8). Linear combinations of those states with different amplitudes and phases include for example all electron wave packets which are rotated by an angle θ about the z-axis (see left panels in Figure 10 for linear polarization) and, in addition, the non-cylinder symmetric states (right panels in Figure 10 for elliptical polarization) [76]. Because the absorption of each elliptically polarized photon alters the m quantum number by $\Delta m = \pm 1$ there are 18 discernible quantum pathways available to excite a superposition state. Using the notation $l(m)$ for a state with the quantum numbers l and m we can write down the involved pathways explicitly: there are eight pathways for the $s \rightarrow p \rightarrow d \rightarrow f$ ladder, i.e. $s(0) \rightarrow p(-1,1) \rightarrow d(-2,0,2) \rightarrow f(-3,-1,1,3)$, six for the $s \rightarrow p \rightarrow d \rightarrow p$ ladder, i.e. $s(0) \rightarrow p(-1,1) \rightarrow d(-2,0,2) \rightarrow p(-1,1)$ and additional four pathways $s(0) \rightarrow p(-1,1) \rightarrow s(0) \rightarrow p(-1,1)$ for the $s \rightarrow p \rightarrow s \rightarrow p$ ladder. The probability for a specific transition is controlled by the corresponding matrix elements and the time-dependent ellipticity of the laser polarization. The amplitudes and phases

of a single continuum state (say for instance $f(m = -1)$) are determined by the interference of all allowed pathways (in this case three) for multiphoton ionization. The initial shape of the electron wave packets after the interaction with the pulse is controlled by the amplitudes and phases of all six contributing specific continuum states shown in Figure 8.
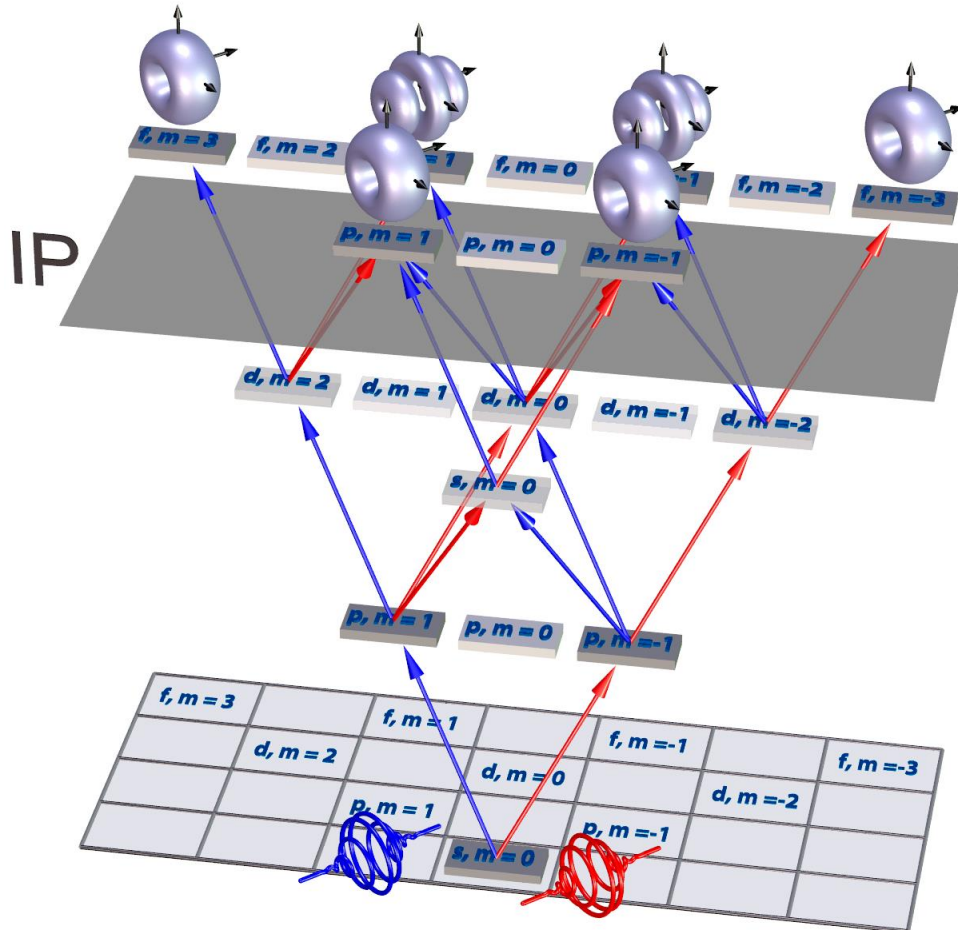

Figure 8 Allowed pathways for multiphoton ionization with elliptically (i.e. a superposition of left- and right-handed circularly) polarized light. The six specific accessible states $f(-3, -1, 1, 3)$ and $p(-1, 1)$ above the ionization potential (IP) interfere to create the designer electron wave packets. Their contributions are determined by the interplay between the time-dependent instantaneous polarization of the laser pulse and the amplitudes and phases of the transition matrix elements. For simplicity, the electron spin is not considered.

Interference in the continuum

In addition to the above mentioned interference effects during the creation of the superposition states in the continuum, the propagation of the electron wave packet will alter the radial shape of the wave packet on its way to the detector.

Analogous to the two interfering partial wave packets in the double pulse experiment shown in Figure 7 many different partial wave packets generated by the shaped laser pulse will interfere during their coherent time evolution. For example, wave packets composed of different angular momentum states which are initially separated radially will mix during the propagation giving rise to the complex wave packets observed in the experiment (see Figure 12).

Determination of transition matrix elements

In the above experiments the instantaneous ellipticity of the pulse (see Section 2.1.6) was used as a control parameter to manipulate the electron wave packet. For the theoretical description of this interaction one needs to have complete knowledge of the involved matrix elements. Because the interference of all those pathways is determined by the different amplitudes and phases of the matrix elements, we can turn the tables, and use the measurement of a shaped free electron wave packet to achieve a complete description of the photo-ionization process in terms of transition amplitudes and phases [108]. In a recent theoretical study incorporating the intra-pulse electronic dynamics a full set of ionization matrix elements for potassium atoms was extracted from extensive experimental data sets on the ionization of potassium atoms with elliptically polarized light [107]. In addition, in that work, three-dimensional photoelectron angular distributions (3dPADs) generated from the extracted matrix elements were compared to experimental, tomographically reconstructed 3dPADs. This technique provides a route to "complete" photo-ionization experiments. Most likely, the technique to determine matrix elements can be refined by employing polarization-shaped pulses which are specifically adapted to this purpose.

3.2.2. Tomographic reconstruction

In this section we will portray a novel technique to measure the three-dimensional shape of free electron wave packets based on a combination of Velocity Map Imaging (VMI) and tomographic reconstruction. Numerous highly differential schemes for the detection of 3dPADs have been developed (see for

instance [108] for a topical review) because they contain detailed information on the intra molecular dynamics and the photo-ionization process. A novel application of photoelectron angular distribution measurements is devoted to probing control of atomic and molecular dynamics [56,109-112] .

Velocity Map Imaging (VMI)

An efficient and yet relatively simple method to measure 3dPADs is to project the complete photoelectron distribution onto a two-dimensional detector plane. An example for this technique is the Velocity Map Imaging (VMI) method [113,114]. In this scheme photoelectrons created in the interaction region are accelerated in the electric field of a parallel-plate capacitor towards a two-dimensional MCP detector. The detector maps the transversal momentum distribution of the 3dPAD. In the quantum mechanical description, the classical motion of an electron in the spectrometer is replaced by the time evolution of a three-dimensional electron wave packet and thus the measurement of a 3dPAD on the two-dimensional MCP detector is described by the Abel transform of the 3dPAD [114,115]. If the photoelectron distribution is cylindrically symmetric a single measurement of a two-dimensional distribution is sufficient to reconstruct the 3dPAD via Abel-inversion provided its symmetry axis lies in the detector plane. The two scenarios for which this condition applies are depicted in Figure 9. For ionization with linearly polarized light it is required that the polarization vector $\vec{E}$ of the light field lies within the detector plane (Figure 9(a)). By contrast, the symmetry axis of a wave packet created with circularly polarized light is the $\vec{k}$-vector. Therefore, in this case the $\vec{k}$-vector needs to be oriented parallel to the detector plane (Figure 9(b)).
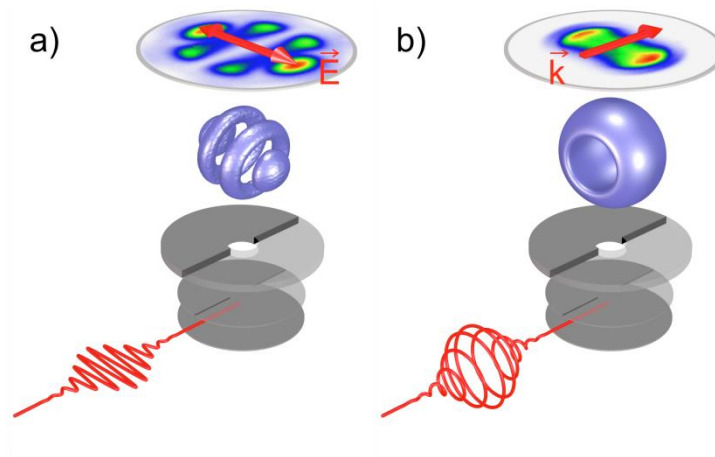
Figure 9 A cylindrically symmetric photoelectron distribution can be reconstructed by the Abel-inversion provided its symmetry axis lies in the detector plane. a) In case of a linearly polarized laser pulse the 3dPAD is cylindrically symmetric about the polarization vector $\vec{E}$ of the light field and hence $\vec{E}$ needs to be in the detector plane. b) The PAD is cylindrically symmetric about the $\vec{k}$-vector if the light field is circularly polarized. For the Abel inversion, the $\vec{k}$-vector needs to be parallel to the detector plane.

Electron wave packets arising from photo-ionization with linearly polarized light being rotated about the z-axis are rotated out of the $y - z$-plane (see left panels in Figure 10 for linear polarization) and therefore, the Abel-inversion is no longer feasible. In addition, wave packets created with elliptically polarized light are no longer cylindrically symmetric (right panels in Figure 10 for elliptical polarization) violating yet another prerequisite for the Abel-inversion. In general, polarization-shaped pulses will lead to complicated 3dPADs without the required symmetry properties necessitating a novel ansatz for reconstruction.

Three-dimensional tomography

Recently, such a novel approach to measuring 3dPADs of arbitrary shape by combination of VMI with tomographic techniques was reported [21,22,106,109]. The idea is based on multiple measurements of two-dimensional projections of the 3dPAD at different angles. To this end, the incoming femtosecond laser pulse –and hence the 3dPAD - is rotated employing a $\lambda/2$ plate. Depending on the complexity of the electron wave packet only a relatively small number of projections need to be recorded for the

reconstruction. In the experiments reported in [22,109] typically 36 projections to cover an angle interval from 0° to 180° were measured. Some representative VMI images measured for the rotation angles $\theta = 0°$, 25°, 45°, 70° and 90° are displayed in Figure 10 along with the reconstructed 3dPAD.
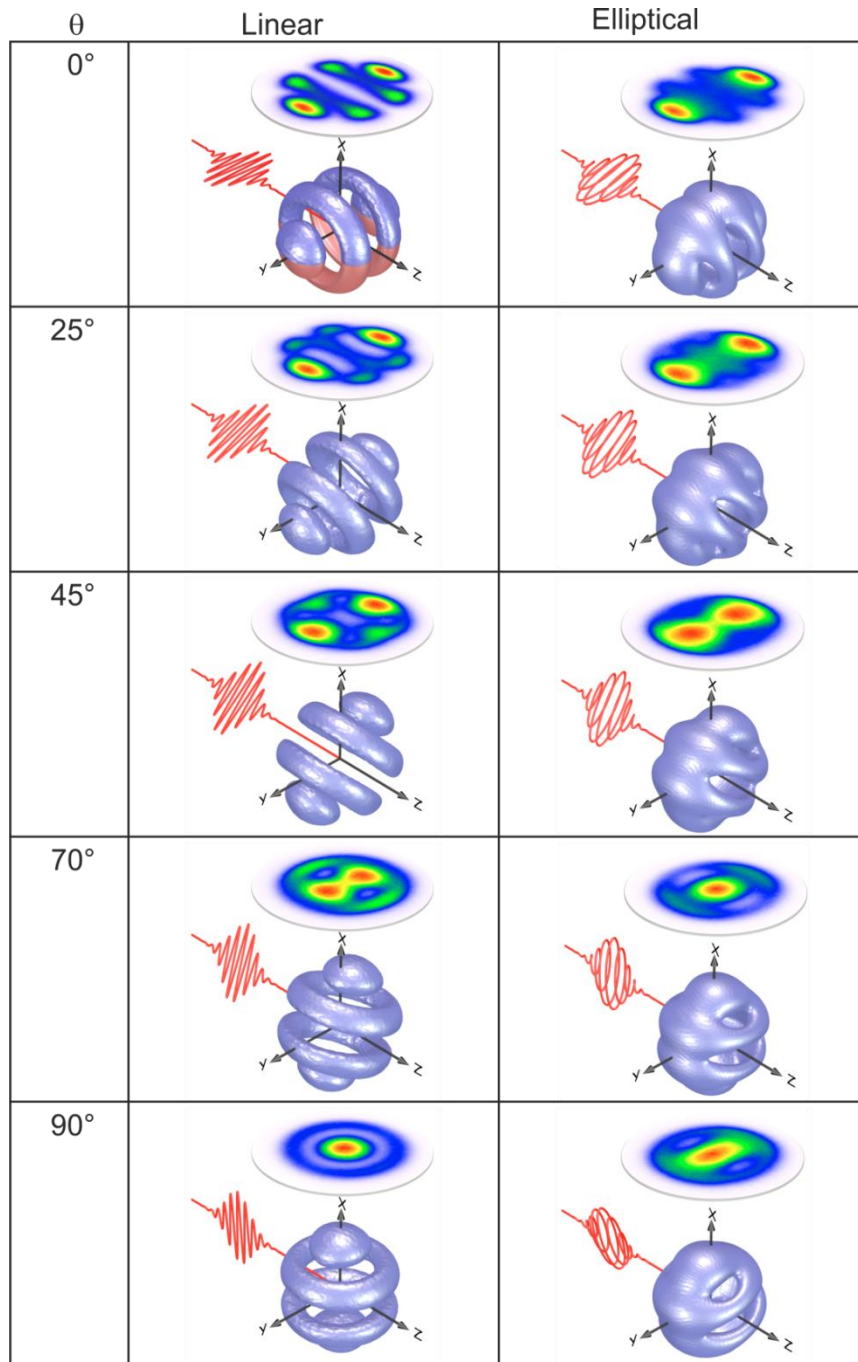

Figure 10 Three-dimensional photoelectron angular distributions (3dPAD) are tomographically reconstructed from measured VMI images. The polarization vector of the ionizing femtosecond laser pulse is rotated about the z-axis by $\theta = 0°$, 25°, 45°, 70° and 90° using a $\lambda/2$ plate. Left: 3dPADs from three-photon ionization of potassium atoms with a linearly polarized femtosecond laser pulse creates an f-type electron

wave packet with little p contribution. The tomographically reconstructed 3dPAD measured at $\theta = 0°$ is compared to the Abel-inverted result (red surface), showing excellent agreement [109]. Right: 3dPADs from elliptical polarization.

Based on the measured data set a tomography algorithm [116] is used to reconstruct the 3dPAD from the measured projections. For the reconstruction no assumptions on the symmetry of the 3dPAD or on details of the ionization mechanism are required. Because a $\lambda/2$ wave plate at an angle of $\theta/2$ rotates any polarization-shaped pulse by an angle of θ this technique is capable of reconstructing electron wave packets from ionization with polarization-shaped laser pulses as well. To see this, we consider the effect of a $\lambda/2$ wave plate at an angle of $\theta/2$ on a polarization-shaped pulse described by Equation (49)

$$J_{\lambda/2}(\theta) \begin{pmatrix} \mathcal{E}_{x,mod}(t) \\ \mathcal{E}_{y,mod}(t) \end{pmatrix} = R(\theta/2)\, J_{\lambda/2}\, R^{-1}(\theta/2) \begin{pmatrix} \mathcal{E}_{x,mod}(t) \\ \mathcal{E}_{y,mod}(t) \end{pmatrix} = R(\theta) \begin{pmatrix} \mathcal{E}_{x,mod}(t) \\ -\mathcal{E}_{y,mod}(t) \end{pmatrix},$$

$$(69)$$

where

$$R(\theta) = \begin{pmatrix} \cos\theta & -\sin\theta \\ \sin\theta & \cos\theta \end{pmatrix} \quad \text{and} \quad J_{\lambda/2} = \begin{pmatrix} 1 & 0 \\ 0 & -1 \end{pmatrix} \qquad (70)$$

denote the matrix of an active rotation about the angle θ and the Jones-matrix for a $\lambda/2$-wave plate, respectively. Note that the y-component changes it sign upon the insertion of the wave plate ($\mathcal{E}_{y,mod}(t) \rightarrow -\mathcal{E}_{y,mod}(t)$). However, since this change-of-sign applies to all rotation angles θ, the tomographic method is unaffected. By insertion of another $\lambda/2$-wave plate at a fixed angle of 0° the change-of-sign could be compensated

$$J(\lambda/2)\, R(\theta/2)\, J(\lambda/2)\, R^{-1}(\theta/2) \begin{pmatrix} \mathcal{E}_{x,mod}(t) \\ \mathcal{E}_{y,mod}(t) \end{pmatrix} = R(\theta) \begin{pmatrix} \mathcal{E}_{x,mod}(t) \\ \mathcal{E}_{y,mod}(t) \end{pmatrix}, \qquad (71)$$

to yield the rotated modulated field. Figure 11 shows the effect of the rotation of a polarization-shaped laser pulse about the propagation axis. Note that in general, if the rotation angle is not a multiple of 90°, the projections look more complicated and thus the underlying spectral modulation function is not easily identified.
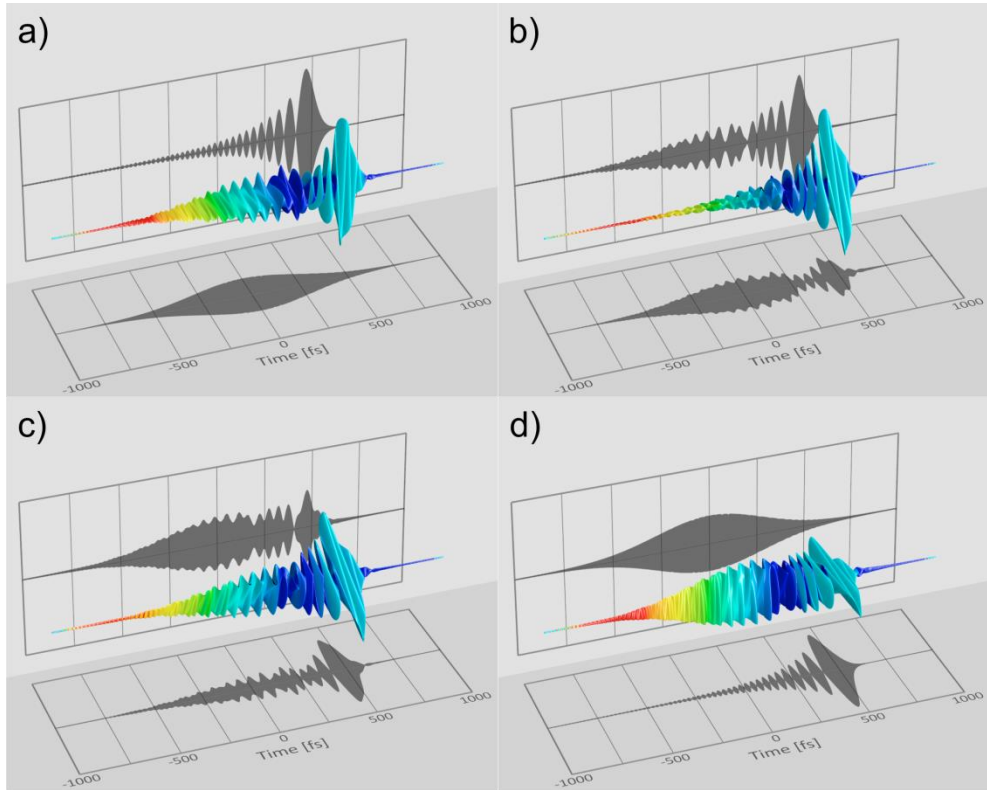
Figure 11 Rotation of a polarization-shaped laser pulse created by GDD and TOD in the two different polarization directions ($\varphi_x(\omega) = \frac{\phi_2}{2!}\omega^2$ and $\varphi_y(\omega) = \phi_1\omega + \frac{\phi_3}{3!}\omega^3$ with $\phi_1 = 500$ fs, $\phi_2 = 5000$ fs^2 and $\phi_3 = -32000$ fs^3). The rotation angles about the z-axis are 0°, 30°, 60° and 90° from a) to d). As described above, the rotation could be implemented experimentally by using a $\lambda/2$ plate. In general, rotation of the pulse leads to projections (black shadows) which appear more complicated.

The electron wave packet generated by ionization with a linearly polarized laser pulse was used to validate this procedure [109]. The two iso-surfaces in the left upper panel of Figure 10 at an angle of $\theta = 0°$ show a comparison of the Abel-inverted results (red iso-surface) with the full tomographic reconstruction (bluish iso-surface). The excellent agreement between both techniques confirms the validity of the approach. Lately, this tomographic technique for reconstruction of the three-dimensional momentum distribution has been implemented to study strong-field multiphoton ionization of argon [117], the alignment of naphthalene molecules [112] and the photoelectron angular distributions from rotationally state-selected ammonia [118].

3.2.3. Designer wave packets

In the previous section, we have discussed the physical mechanism of multiphoton excitation with polarization-shaped femtosecond laser pulses and an experimental technique to reconstruct three-dimensional free electron wave packets. We now turn to experiments devoted to the creation of particularly complex shaped electron wave packets in the continuum – so-called designer electron wave packets [22,106] - by making use of the electronic structure of atoms together with polarization-shaped laser pulses. The bluish iso-surface shown in Figure 12 (a) is an example for such a designed electron wave packet in the continuum. This complex electron wave packet was created by REMPI of potassium atoms employing combined "V"-shaped spectral phase modulation and polarization shaping (Figure 12 (b)). The "V"-shaped spectral phase advances the intense red spectral band and retards the weaker blue spectral band [20,55]. Due to the additional phase jump, the first red detuned pulse is linearly polarized along the x-axis whereas the second blue detuned pulse is circularly polarized. The cut through the distribution in Figure 12 (c) shows the interior of the complex three-dimensional distribution. In addition, the energy calibrated electron distributions in the three central planes are projected out.
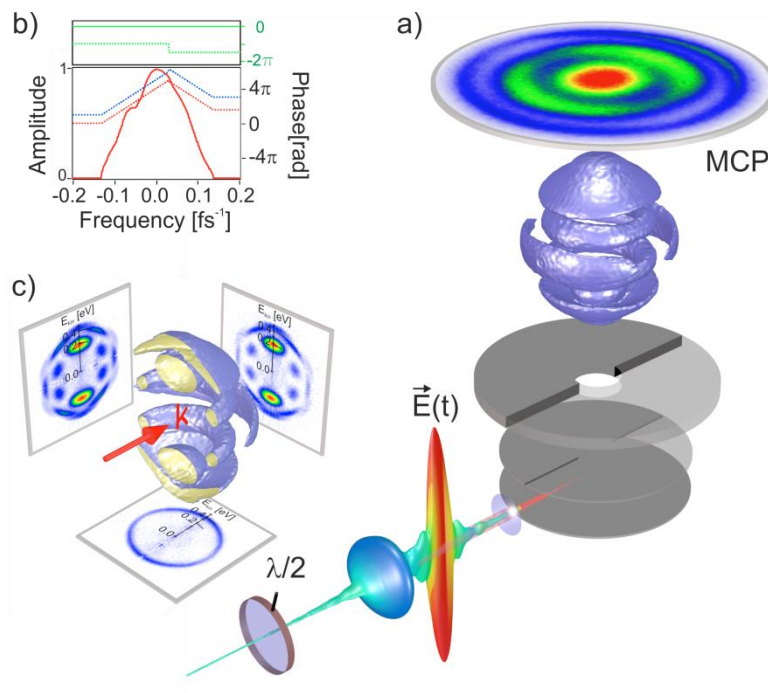

Figure 12 Designer free electron wave packet. a) Three-dimensional tomographic reconstruction of the electron wave packet. b) "V"-shaped phase in the frequency

domain. The central wavelength of the pulse is 790 nm, the FWHM pulse duration 30 fs and the peak intensity about 4 x 10^{12} W/cm². (c) Cut through the distribution along with the electron distributions in the three central planes.

3.2.4. Adaptive optimization by polarization shaping

As discussed above, adaptive optimization is a powerful tool to find suitable laser pulses for coherent control. In most applications reported in the literature so far, linearly polarized femtosecond laser pulses were used for the optimization procedure. In this section we discuss two examples of coherent control by adaptive optimization of polarization-shaped laser pulses.

3.2.4.1. Diatomic molecules

Soon after the introduction of polarization shaping by Brixner et al. [73] this technique was applied to coherent control of two-photon absorption in atomic rubidium by investigating the atom's fluorescence [74]. The maximization of the ion yield in the REMPI of potassium molecules was the first demonstration of adaptive optimization of molecular dynamics using polarization-shaped femtosecond laser pulses [75]. In that work it was established that polarization-shaped laser pulses increase the ionization yield beyond that obtained with an optimally shaped linearly polarized laser pulse. Figure 13 (a) shows comparative optimizations of the K_2^+ yield proving that polarization shaping is superior to phase-only shaping. The inset to Figure 13 (a) shows an example of an optimal laser pulse – shaped in phase and polarization – along with the two orthogonal polarization components represented by black shadows. The physical rationalization of this observation is related to the adaptation of the vectorial electric field to the time evolution of the relevant vectorial transition dipole moments. In particular, the different multiphoton ionization pathways in K_2, involving parallel ($A^1\Sigma_u^+ \leftarrow X^1\Sigma_g^+$) and perpendicular ($2^1\Pi_g \leftarrow A^1\Sigma_u^+$) dipole transitions (Figure 13 (b)) favor different polarization directions of the exciting laser field during the interaction.
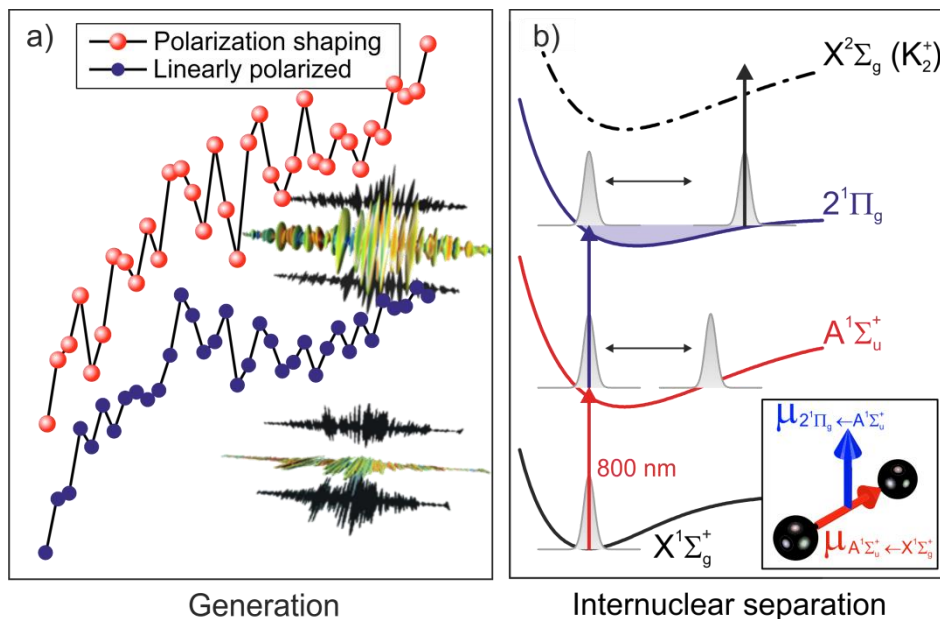
Figure 13 a) Comparative adaptive optimizations of the K_2^+ yield and an example of an optimal laser pulse – shaped in phase (lower panel) and in phase and polarization (upper panel). b) The excitation scheme shows that different multiphoton ionization pathways involve parallel ($A^1\Sigma_u^+ \leftarrow X^1\Sigma_g^+$) and perpendicular ($2^1\Pi_g \leftarrow A^1\Sigma_u^+$) dipole transitions.

3.2.4.2. Designer electron wave packets

The two-dimensional projections of the electron wave packets shown in Figures 10 and 12 are quite varied and complex. However, recently it was shown experimentally that it is even possible to manipulate the three-dimensional electron wave packet such that an arbitrarily shaped target projection (which is compatible with energy conservation and the symmetry of the photo-ionization process) can be obtained by suitable optimization of the shaped ionization pulse [21]. To this end, the two-dimensional dumbbell-shaped target projection shown in Figure 14 was defined (the boxed target image is labeled with T). During the optimization the target is iteratively approximated by adaption of the spectral phases of the laser pulse. The sequence (1-5) in Figure 14 shows the evolution of the measured projections towards the target (T) during the optimization procedure. While the measurements of the first generation (1) have some similarity with the projection of an f-electron wave packet, see for example Figure 10 (a) for linear polarization, in (2-3) the outer maxima of

the dumbbell start to emerge. In the course of the optimization procedure the inner part of the dumbbell is filled (4-5) such that eventually the measured projection converges to the target function.
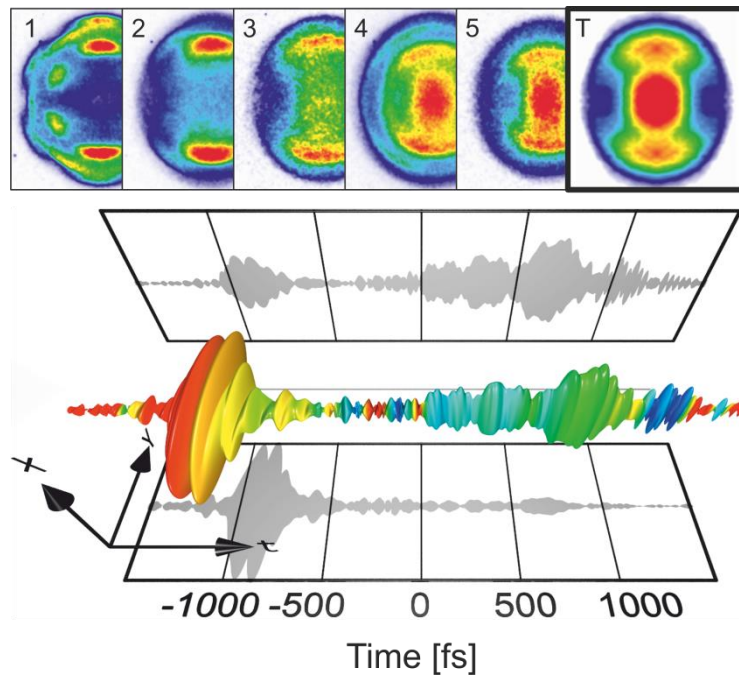

Figure 14 Adaptive optimization of photoelectron angular distribution (PAD) measured by velocity map imaging (VMI) from REMPI of potassium atoms with polarization-shaped femtosecond laser pulses employing an evolutionary algorithm. The pulse parameters are: central wavelength of 790 nm, FWHM pulse duration of 30 fs and peak intensity of about 3×10^{11} W/cm^2.

For the optimization, the spectral phase modulation function was parameterized by piecewise linear functions in order to delay different spectral bands with respect to each other and, in addition, a relative phase between both polarization components was applied in order to control the ellipticity of individual spectral bands.

3.3. Strong field control

The use of intense laser fields is a prerequisite for efficient atomic and molecular excitation. Strong-field interactions beyond the perturbative regime offer a rich variety of laser-induced excitations and enable new physical mechanisms to control the ensuing dynamics. In particular, strong fields alter the potential energy landscape of an atom or a molecule by means of the dynamic (AC) Stark effect. The new light-induced potentials form the stage for non-perturbative quantum dynamics and open new excitation pathways to target channels which are inaccessible in weak laser fields. In this section we focus on strong-field control experiments on model systems which allow the analysis of the underlying physical mechanisms by comparison with simulations. Physical mechanisms to direct the strong-field induced quantum dynamics comprise – in addition to the interference of multiple excitation pathways discussed in Section 3.2 – resonant and off-resonant Dynamic Stark Shifts (DSSs) [56,119-121], Adiabatic Passage techniques such as RAP (Rapid Adiabatic Passage) and STIRAP (Stimulated Raman Adiabatic Passage) [122-124] and multi-pulse scenarios like Photon Locking (PL) [9,105,125-128] being the optical analogue of Spin Locking [129,130] known from NMR. A common basis for all of these mechanisms is the Selective Population of Dressed States (SPODS) [67,105]. In the following we will review these techniques and highlight their potential for efficient ultrafast switching of population transfer among different target states.

3.3.1 Dynamic Stark shifts

A general characteristic of strong-field laser-matter interactions are energy shifts of quantum states due to the dynamic Stark effect. Precisely timed dynamic Stark shifts can be used as a tool to open or close certain excitation pathways during the interaction and hence steer the population flow into preselected target channels. The off-resonant dynamic Stark effect for instance, which acts on the time-scale of the intensity envelope of the laser pulse, was exploited to control the branching ratio of a non-adiabatic photodissociation reaction in IBr molecules [121]. In cases where undesired dynamic Stark shifts impede the excitation of the target state ultrafast pulse shaping techniques can be employed to counteract the effect and optimize the transition probability

[120]. For example, ultrafast efficient switching of population transfer among different target states in Na atoms using intense chirped laser pulses was demonstrated [56]. It was shown that the physical mechanism governing the control was based on the interplay of RAP (cf. Section 3.3.3) and DSSs. Figure 15(a) shows the excitation and ionization scheme of Na interacting with intense $\Delta t = 30$ fs FWHM, $\lambda_0 = 795$ nm laser pulses.
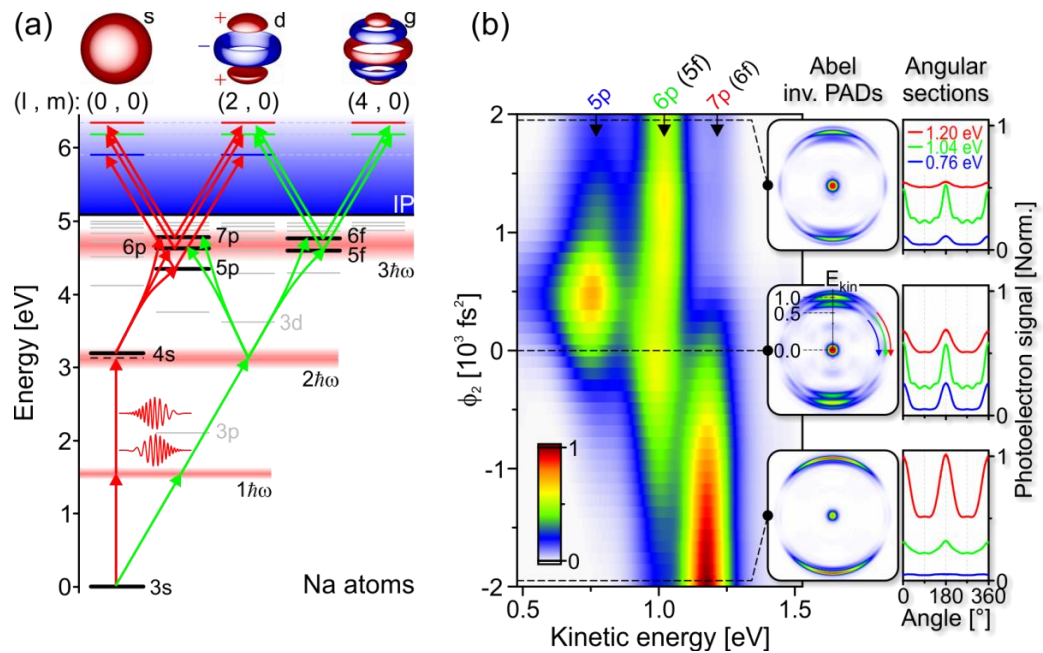

Figure15 (a) Scheme for simultaneous excitation and ionization of Na atoms by ultrashort chirped laser pulses. Red horizontal bars indicate the first, second and third order laser spectrum, respectively. Red and green arrows indicate the predominant REMPI channels. Photoelectron wave packets from these channels are characterized by distinct symmetries illustrated by the spatial electron density distributions on top. (b) Measured photoelectron spectra from strong-field REMPI of Na by intense chirped laser pulses. Insets: Abel inverted PADs for distinct values of ϕ_2 and angular sections at three kinetic energies corresponding to the three main ionization channels around 0.76 eV ($5p$), 1.0 eV ($6p/5f$) and 1.2 eV ($7p/6f$), respectively. The weak f-type contribution observed around 0.2 eV in the middle PAD has been discussed in terms of two-photon ionization from the transiently populated "virtual" state $3p$ [56].

Red and green arrows highlight the most relevant REMPI channels. The dominant pathway is (2+1+1) REMPI involving the strongly driven two-photon resonance $4s \leftarrow\leftarrow 3s$ and ionization via the high-lying target states $5p$, $6p$ and

$7p$. Photoelectrons from this ionization channel are characterized by a combined s- and d-symmetry and kinetic energies of 0.76 eV ($5p$), 1.0 eV ($6p$) and 1.2 eV ($7p$), respectively. A competing pathway is the (3+1) REMPI process which proceeds via the high-lying target states $5f$ and $6f$. This ionization channel gives rise to photoelectrons wave packets with combined d- and g-symmetry and kinetic energies of 1.0 eV ($5f$) and 1.2 eV ($6f$). Since all excitations are driven coherently by the same laser pulse, photoelectron wave packets launched with the same kinetic energy interfere in the continuum. PADs measured in the experiment unambiguously reflect the symmetries of the photoelectron wave packets and thus provide direct information on the underlying ionization channel. Figure 15(b) shows photoelectron spectra from strong-field excitation and ionization of Na with linearly polarized chirped laser pulses (cf. Equation (30) and see Figure 1(a)) as a function of the spectral chirp parameter ϕ_2 ranging from -2000 to $+2000$ fs^2. The intensity of the input pulse was $I_0 = 1 \times 10^{13}$ W/cm^2. For clarity all spectra are presented with energy-resolution. Selected spectra shown in the insets are presented with angular resolution in addition. The experiment demonstrates that a single control parameter, i.e. the chirp, can be sufficient to switch the atomic excitation between different target states. For the bandwidth limited pulse, i.e. $\phi_2 = 0$, three contributions appear in the spectrum with similar intensity. Due to its combined s- and d-symmetry the signal at 1.2 eV is assigned to ionization from target state $7p$. The signal at 1.0 eV exhibits a pronounced g-symmetry and thus originates from target state $5f$. The d-symmetry of the signal at 0.76 eV finally suggests ionization from target state $5p$. For large negative values of ϕ_2 the contribution from the p-channel at 1.2 eV is considerably enhanced whereas the 1.0 eV contribution is strongly suppressed and the 0.76 eV contribution has essentially vanished from the spectrum. This observation indicates the selective excitation of the target state $7p$ by down-chirped laser pulses. Upon inversion of the chirp however, the p-channel is largely suppressed. For large positive values of ϕ_2 the PAD is dominated by the contribution from the f-channel at 1.0 eV, indicating the selective excitation of the target state $5f$ by up-chirped laser pulses. A third prominent region opens

up for small positive values of ϕ_2. Here the low energy contribution at 0.76 eV assigned to excitation of and ionization from target state $5p$ is most pronounced. This target state is completely non-resonant with the (third order) laser spectrum and therefore utterly inaccessible in the weak-field regime. Its efficient excitation requires a strong DSS resulting from the interaction with short and intense laser pulses, but is optimized by application of a moderate up-chirp.
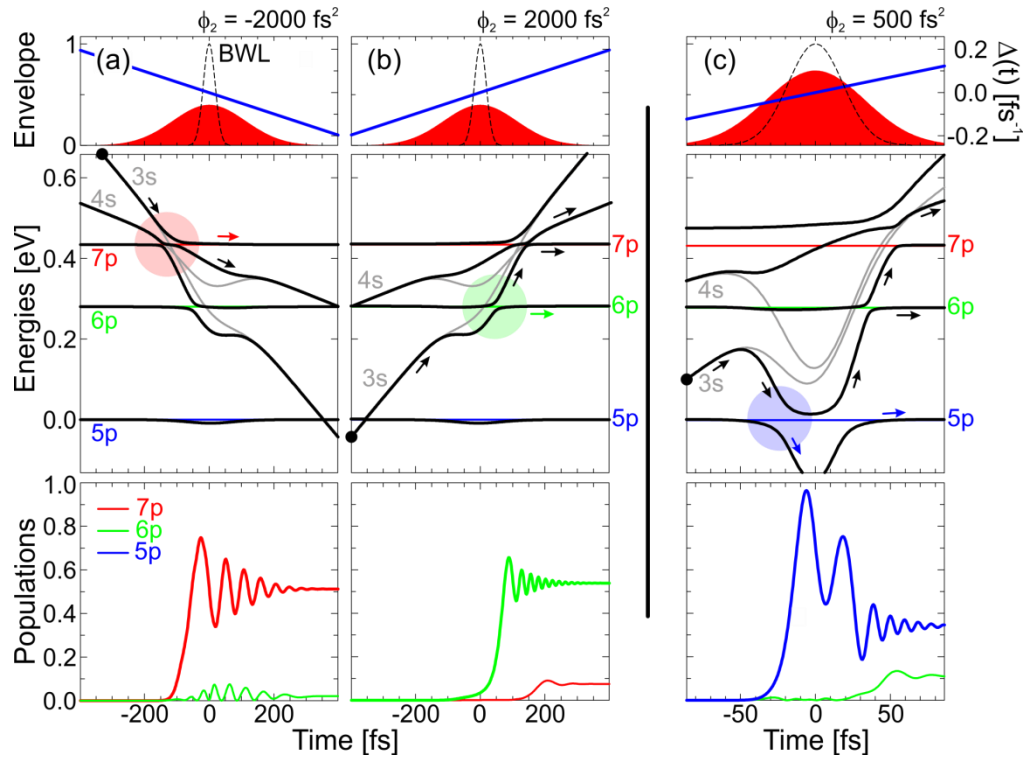

Figure 16 Calculated neutral excitation dynamics of Na atoms interacting with intense chirped Gaussian-shaped laser pulses. The laser pulses are shown in the top frames, decomposed into their temporal envelope $\mathcal{E}(t)$ (red background) and detuning $\Delta(t)$ (blue line). In the middle frames grey and coloured lines display the time-dependent bare states of the Na five-state-system. Black lines indicate the adiabatic or dressed atomic states resulting from diagonalization of the system. The black dots mark the respective initial conditions while arrows serve to trace the major population flow. The bottom frames show the population dynamics of the relevant target states under the different excitation conditions. Note the different time-axis in (c).

In order to gain insights into the physical mechanisms behind the observed population control, quantum dynamics simulations were carried out by solving the Time-Dependent Schrödinger Equation (TDSE). For simplicity the Na atom

was modelled by a five-state-system considering only the p-channel. A selection of numerical results is shown in Figure 16. The middle row shows the energy scheme of the five-state-system in a quantum mechanical frame rotating with the instantaneous laser frequency. In this frame, the eigenenergies of the two-photon resonant states $3s$ and $4s$ (grey lines) are chirped due to both the linear detuning $\Delta(t)$ (cf. Equation (36)) of the pulse and pronounced DSSs induced by the non-resonant intermediate state $3p$. These time-variations give rise to various level crossings (dynamic resonances) with the target states $5p$, $6p$ and $7p$ during the course of the interaction. For example, in the case of down-chirped pulses with $\phi_2 = -2000$ fs^2 shown in Figure 16(a) a three-state bow-tie crossing between states $3s$, $4s$ and $7p$ around $t = -130$ fs (light-red circle) is responsible for the efficient excitation of the target state $7p$. Because the interaction is adiabatic (cf. Section 3.3.3) the interacting system follows the upper adiabatic state (upper black line) starting at the ground state $3s$ and reaching the upper target state $7p$ after the avoided crossing. For up-chirped pulses with $\phi_2 = +2000$ fs^2 shown in Figure 16(b) the energy scheme is time-reversed. In this case the avoided crossing between ground state $3s$ and target state $6p$ around $t = 50$ fs (light-green circle) is crucial to the excitation. Again adiabatic interaction determines the course of the population flow steering the system into the intermediate target state $6p$. In the third case, moderately up-chirped pulses with $\phi_2 = 500$ fs^2 shown in Figure 16(c), the laser pulse is much shorter and more intense. This results in stronger and more rapid dynamic Stark chirps creating non-adiabatic, impulsive excitation conditions. The population flow is governed by a Stark chirp induced dynamic resonance between the dressed ground state $3s$ and the target state $5p$ around $t = -25$ fs (light-blue circle). Here adiabaticity is broken leading to an efficient population transfer among the adiabatic states, and eventually into the lower and far off-resonant target state $5p$.

In conclusion, the results presented on strong-field REMPI of Na atoms demonstrate that in strong-field control multiple pathways involving different physical mechanisms are generally at play simultaneously. Here an interplay of adiabatic passage and dynamic Stark shifts induced by a strongly driven two-

photon resonance was identified to control the population transfer along different excitation pathways using the chirp as a single control parameter.

3.3.2 Selective Population of Dressed States

The essence of strong-field coherent control is the manipulation of dressed state energies and populations [67,105]. In order to unravel the physical mechanisms underlying dressed state control we start by an analysis of the interaction of intense shaped femtosecond laser pulses with a simple well-defined model system. Two-state atoms serve as an approximation to suitably chosen real systems, which is particularly justified in the case of resonant excitation. The advantage of one-photon resonances – as compared to multi-photon resonances (cf. Section 3.3.1) or non-resonant excitation – are the strong laser-induced couplings enabling highly efficient excitation. Even at moderate laser intensities non-perturbative dynamics are readily achieved. Moreover, in the resonant case the dynamic Stark effect gives rise to energy splittings rather than unidirectional energy shifts. These so-called Autler-Townes (AT) splittings [131] allow controlled bipolar energy shifts in the order of several 100 meV [67]. As an example, we consider the excitation of K atoms by ultrashort near-infrared laser pulses, as sketched in Figure 17. The laser resonantly couples the states $4s$ and $4p$, and simultaneously ionizes the atom in a non-resonant two-photon process. In the weak-field limit (a) this (1+2) REMPI gives rise to a single peak in the photoelectron spectrum mapping the energy and the population of the $4p$ bare state into the ionization continuum. Since the interaction is perturbative the ground state population remains essentially unaltered and the population transfer to the continuum is negligibly small. In the strong-field regime however, Rabi-cycling in the resonant two-state system causes a splitting of the photoelectron peak into the AT doublet. The origin of this splitting is readily understood in the dressed state picture. In the presence of an intense resonant laser field $\mathcal{E}(t)$ the dressed states of the strongly driven
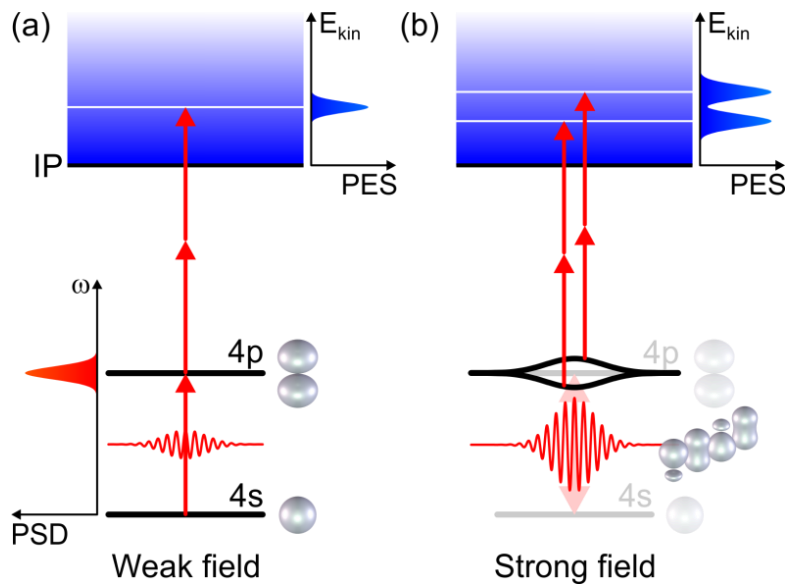
Figure 17 Resonant excitation and simultaneous ionization of a two-state atom (K) by a bandwidth-limited laser pulse. (a) In the weak-field limit the atom is photoionized in a (1+2) REMPI process giving rise to a single peak in the energy-resolved photoelectron spectrum. (b) In the strong-field regime this peak splits into the Autler-Townes (AT) doublet due to Rabi-cycling in the strongly driven neutral system. Here, photoionization maps the dressed states rather than the bare states into the ionization continuum and acts as a sensitive probe for the dressed state energies (AT splitting) and populations (AT contrast).

two-state atom repel each other. This repulsion results in an energy splitting of $\hbar\Omega(t) = \mu\mathcal{E}(t)$, where $\Omega(t)$ denotes the Rabi frequency and μ is the electric dipole moment of the transition $4p \leftarrow 4s$. Photoionization maps the *interacting* system, i.e. the dressed states, into the photoelectron spectrum [39]. As a result, two new channels open up in the continuum with energies corresponding to the dressed state energies, and a branching ratio determined by the dressed state populations. Hence, the photoelectrons act as a sensitive probe for the strong-field induced dynamics of dressed states in terms of both energy (AT splitting) and population (AT contrast).

While the manipulation of the dressed state energies is rather straight forward as their splitting follows the temporal envelope of the laser field $\mathcal{E}(t)$, controlling the populations of dressed states is somewhat more sophisticated. The semiclassical spatiotemporal description of the interaction of the atom with an intense resonant laser pulse provides an intuitive physical picture of dressed

state population control. The rapidly oscillating laser field $E(t)$ couples to the valence electrons, distorts the spatial electron distribution and induces an oscillating electric dipole moment $\langle\mu\rangle(t)$. Under resonant excitation conditions the induced dipole follows the driving field with a phase shift of $-\frac{\pi}{2}$, in full analogy to a classical driven oscillator. Hence the interaction energy $\langle\mathcal{V}\rangle(t) = -\langle\mu\rangle(t) \cdot E(t)$ of the dipole in the external driving field vanishes on the time average. Recalling that quantum mechanically the dressed states are the eigenstates of the interacting system, i.e. of the interaction operator $\boldsymbol{\mathcal{V}}(t) = -\boldsymbol{\mu} \cdot E(t)$, a vanishing interaction energy implies equal population of upper and lower dressed state (no selectivity). In order to accomplish the selective population of a single dressed state, the interaction energy needs to be either maximized (upper dressed state) or minimized (lower dressed state). This requires (i) the preparation of a dipole $\langle\mu\rangle(t)$ oscillating with maximum amplitude and (ii) suitable phase matching of the induced charge oscillation and the driving laser field $E(t)$. In-phase oscillation of laser and dipole leads to a minimization of $\langle\mathcal{V}\rangle(t)$, whereas out-of-phase oscillation of both maximizes $\langle\mathcal{V}\rangle(t)$.

In summary, the key to the control of dressed state populations is the interplay of the optical phase of the laser and the quantum mechanical phase of the induced charge oscillation prepared in a state of maximum coherence. The next sections present two different ways to realize these conditions in order to achieve the Selective Population of Dressed States (SPODS).

3.3.3 SPODS via Rapid Adiabatic Passage

In this section we follow up on Section 3.3.1 and discuss the resonant excitation of two-state atoms by intense chirped laser pulses. Again the K atom is analysed as a prototype of a two-state system interacting with chirped pulses [54]. Figure 18 shows energy-resolved photoelectron spectra measured by simultaneous excitation and ionization of K atoms with ultrashort near-infrared laser pulses ($\Delta t = 30$ fs, $\lambda_0 = 795$ nm, $I_0 = 4 \times 10^{11}$ W/cm²) chirped according to Equation (30). The spectra show the AT doublet for different values of the spectral chirp parameter ϕ_2 ranging from -1600 fs² to 1600 fs² (see also Figure

1(a)). For the unmodulated pulse, i.e. $\phi_2 = 0$, the spectrum exhibits both AT components – the slow electrons at $E_{kin} = 0.30$ eV and the fast electrons at $E_{kin} = 0.45$ eV – with nearly the same intensity. The resonant bandwidth-limited pulse populates both dressed states in equal measure, achieving no selectivity. For $\phi_2 > 0$ however, the asymmetry of the AT doublet shifts towards the low energetic component. Already at moderate chirp values of around $\phi_2 = 500$ fs² the high energetic component has vanished completely from the spectrum, indicating the selective population of the lower dressed state by the up-chirped laser pulse. The overall decrease in photoelectron yield is due to the lowered peak intensity of chirped pulses, which impairs the two-photon ionization probability. For down-chirped pulses around $\phi_2 = -500$ fs² the whole picture is inverted. Here the AT doublet is dominated by the fast photoelectrons whereas the slow electrons are completely suppressed. In this case the upper dressed state is populated selectively.
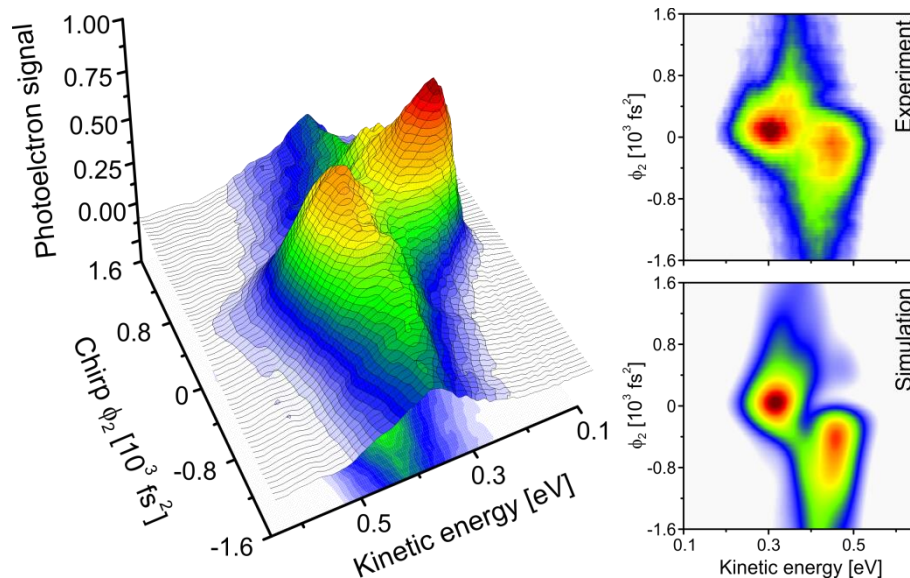

Figure 18 Energy-resolved photoelectron spectra from simultaneous excitation and ionization of K atoms with intense resonant chirped femtosecond laser pulses. The spectra show the AT doublet as a function of spectral chirp parameter ϕ_2. For large positive chirp values (up-chirped pulses) exclusively slow photoelectrons are detected, which indicates the selective population of the lower dressed state in the neutral atom. Upon inversion of the chirp, the photoelectrons switch from the lower to the upper ionization channel. Down-chirped laser pulses promote the fast electrons, indicating the selective population of the upper dressed state.

In order to analyze the physical mechanism the TDSE is solved numerically for a two-state atom interacting with intense resonant chirped laser pulses, including two-photon ionization from the $4p$ state [39]. Figure 19 shows calculation results for the case of an up-chirped laser pulse. The pulse is shown in frame (a). Frame (b) displays the population dynamics of the ground state $|s\rangle$ (dashed black line) and excited state $|p\rangle$ (dashed-dotted grey line), along with those of the corresponding lower dressed state $|l\rangle$ (solid blue line) and upper dressed state $|u\rangle$ (solid green line). The induced dipole $\langle\mu\rangle(t)$, i.e. the expectation value of the dipole operator $\boldsymbol{\mu}$, is shown in frame (c) and compared to the driving electric field $E(t)$ (grey line), and finally frame (d) shows the expectation value $\langle\mathcal{V}\rangle(t)$ (black line) of the interaction operator $\boldsymbol{\mathcal{V}}(t) = -\boldsymbol{\mu}\cdot E(t)$ together with the eigenenergies $\varepsilon_l(t)$ of the lower dressed state (blue line) and $\varepsilon_u(t)$ of the upper dressed state (green line). Snapshots of the spatiotemporal electron density dynamics $\varrho(\boldsymbol{r}, t)$ are shown on top of the figure to visualize the relation of the induced electric dipole (blue arrows) and the driving electric field (red arrows). Initially the atom is in the ground state $|s\rangle$ characterized by a spherically symmetric s-wave. The dipole moment of this electron distribution vanishes exactly and so does the interaction energy. Therefore, the dressed states are equally populated prior to the interaction. Excitation of the atom gradually launches the coherent charge oscillation which follows the driving field strictly in-phase due to the initial red-detuning of the up-chirped pulse with respect to the atomic resonance. Because the variation of the field in terms of amplitude and instantaneous frequency is sufficiently slow, the dipole follows the field adiabatically so that the initial phase relation is maintained throughout the entire interaction. Thus the phase matching condition is automatically fulfilled. As the dipole gains amplitude the interaction energy is successively lowered and the equal population of dressed states is lifted in favour of the lower dressed state. However, it is not before the dipole oscillation reaches maximum amplitude that full selectivity is attained. This condition is fulfilled around $t = 0$ where the bare states approach the state of maximum electronic coherence. In this time window the interaction energy $\langle\mathcal{V}\rangle(t)$ is minimized and its time average coincides exactly with the energy of the lower dressed state.
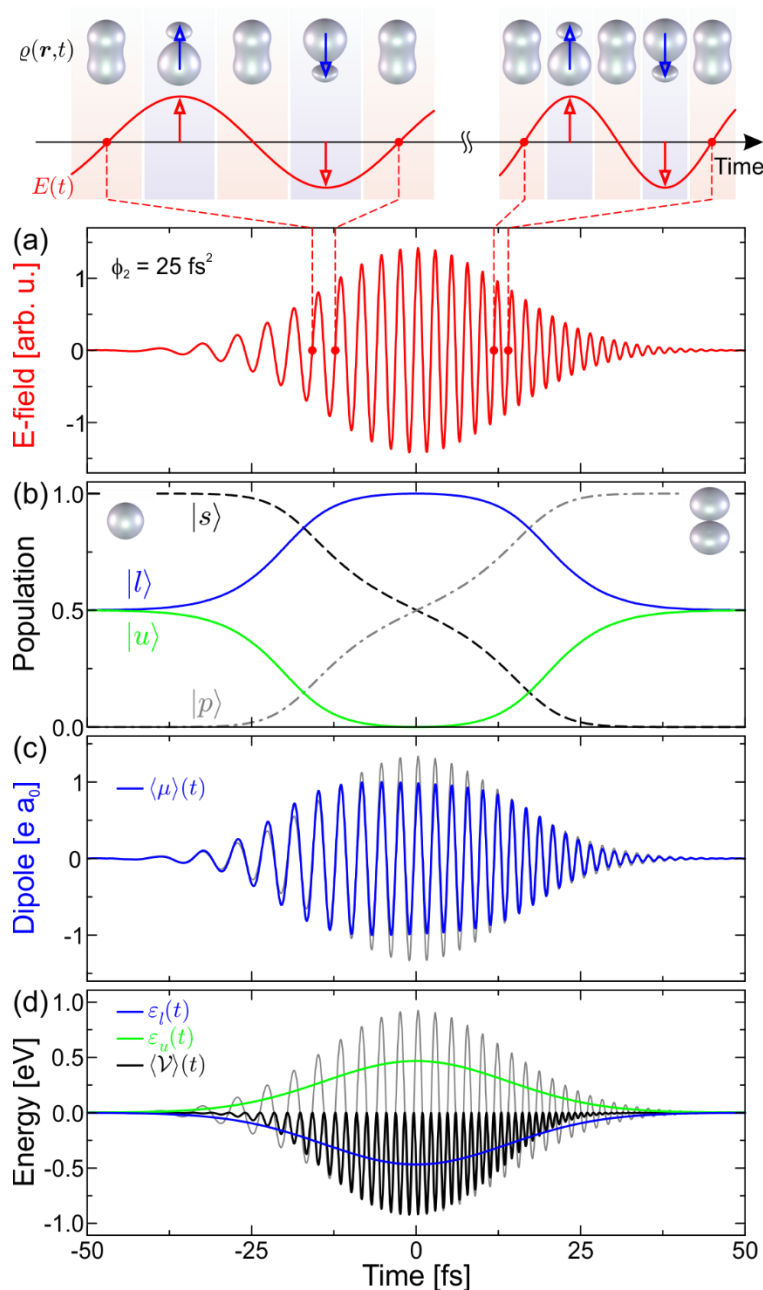
Figure 19 Selective population of the lower dressed state via RAP using a chirped laser pulse. (a) Electric field $E(t)$ of the up-chirped pulse. (b) Calculated population dynamics of the bare states (dashed lines) and dressed states (solid lines) of the neutral two-state atom. (c) Induced electric dipole moment $\langle\mu\rangle(t)$ (blue line) driven by the external laser field (grey line). (d) Eigenenergies of the dressed states (blue line: lower, green line: upper) and interaction energy $\langle\mathcal{V}\rangle(t)$ of the induced dipole in the driving field (black line). The top of the figure shows snapshots of the spatiotemporal electron dynamics during selected cycles of the laser field. The coherent charge oscillation (blue arrows) is strictly in phase with the optical oscillation (red arrows), which is the basis for the selective population of the lower dressed state.

According to the semiclassical picture this indicates selective population of the lower dressed state which is in fact verified by the quantum mechanical population dynamics in (b). Subsequently the pulse continues to excite the atom, steering it adiabatically towards the upper state $|p\rangle$. Because the (permanent) dipole moment of the p-wave vanishes as well, the amplitude of the induced dipole decreases continuously and converges asymptotically towards zero. As a consequence also the interaction energy returns to zero indicating a successive loss of selectivity among the dressed states. By the end of the pulse the dressed state populations are again fully equalized. The adiabatic inversion of a two-state system due to adiabatic following of the field-induced charge oscillation is the spirit of Rapid Adiabatic Passage (RAP) originally developed in NMR [130] and demonstrated in the optical regime on atoms [9,54,123,132,133] and molecules [32,134,135]. With the phase matching condition 'built-in', RAP entails the transient realization of SPODS during the excitation stage of maximum electronic coherence. To conclude, driving quantum systems adiabatically is one distinct method to control the populations of dressed states.

3.3.4 SPODS via Photon Locking

Adiabatic scenarios such as RAP generally rely on long interaction times and large pulse energies. In practice, it is often desirable to act on the fastest possible time scale in order to outperform intramolecular energy redistribution or decoherence processes. A different, non-adiabatic approach to realize SPODS is based on phase-locked sequences of ultrashort pulses. The basic mechanism behind this approach is Photon Locking (PL) [9,105,125-128] analogous to Spin Locking in NMR [129,130]. An experimental demonstration of SPODS via PL on K atoms using multi-pulse sequences from sinusoidal spectral phase modulation (cf. Equation (45) and Figure 2(a)) is shown in Figure 20. The experimental conditions are the same as in Section 3.3.3 except for the laser intensity which was set to 7×10^{11} W/cm². The sine-amplitude was set to $A = 0.3$ rad, the sine-frequency to $T = 120$ fs.
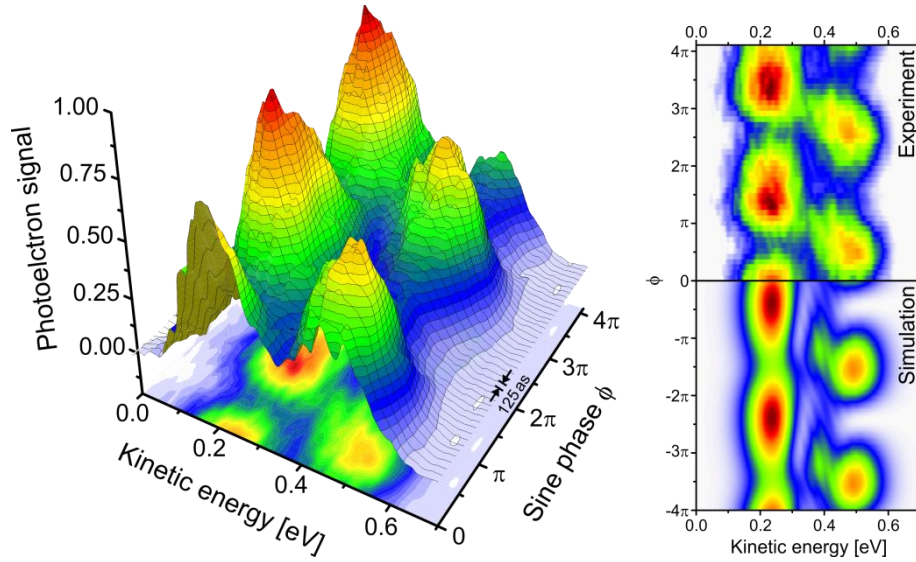
Figure 20 Energy-resolved photoelectron spectra from simultaneous excitation and ionization of K atoms with intense resonant multi-pulse sequences from sinusoidal phase modulation. The spectra show the AT doublet as a function of the sine-phase ϕ which controls the temporal phases of the individual subpulses. As ϕ scans through one optical cycle (2π) the photoelectrons switch back and forth between the two ionization channels. At $\phi = \frac{\pi}{2}$ the spectrum is dominated by fast electrons, indicating the selective population of the upper dressed state. Selective population of the lower dressed state occurs at $\phi = \frac{3\pi}{2}$, i.e. half an optical cycle later, where predominantly slow electrons are detected. The physical mechanism behind the impulsive realization of SPODS via sequences of ultrashort pulses is found to be Photon Locking.

This parameter combination results essentially in a triple-pulse sequence of an intense main pulse preceded by a much weaker prepulse and succeeded by a likewise weak postpulse, with a pulse-to-pulse separation of 120 fs. The temporal phase of the pulse sequence, and hence the interplay between optical and quantum mechanical phase, is controlled by the sine-phase ϕ of the spectral phase function $\varphi_{SIN}(\omega) = A \sin(\omega T + \phi)$ as shown in Figure 2(a). Figure 20 shows energy-resolved photoelectron spectra as a function of ϕ varied over two optical periods. As ϕ scans through one optical cycle the photoelectrons switch back and forth between the two ionization channels. For instance at $\phi = \frac{\pi}{2}$ the AT doublet shows predominantly fast electrons at $E_{kin} = 0.50$ eV while slow electrons at $E_{kin} = 0.25$ eV are strongly suppressed.
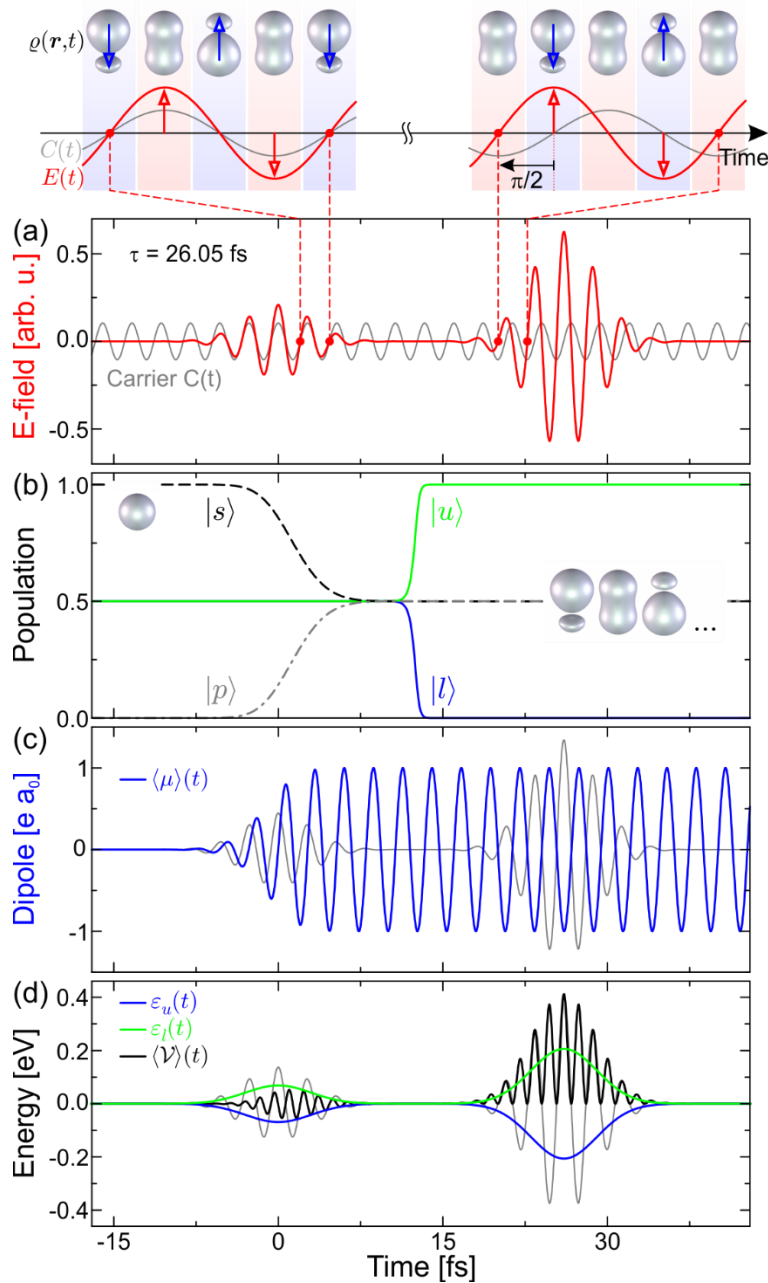
Figure 21 Selective population of the upper dressed state via PL using a sequence of resonant laser pulses. The assignment of the displayed quantities is the same as in Figure 19. The weak prepulse prepares the neutral atom in a state of maximum electronic coherence. Due to the resonant excitation, the induced charge oscillation follows the driving field with a phase shift of $-\frac{\pi}{2}$ as illustrated on the top left side of the figure. The intense main pulse, however, is phase-shifted by $\frac{\pi}{2}$ with respect to the prepulse and hence oscillates in anti-phase with the dipole. Therefore the interaction energy $\langle \mathcal{V} \rangle(t)$ is maximized during the main pulse, which is equivalent to the selective population of the upper dressed state. Note, that the bare state populations are frozen and the charge oscillation remains unaffected by the interaction with the intense resonant main pulse.

Here the upper dressed state is populated selectively. In contrast, half an optical cycle later at $\phi = \frac{3\pi}{2}$ the AT doublet is inverted. Here the slow electrons dominate the spectrum while the fast electrons have essentially vanished, indicating selective population of the lower dressed state. The physical mechanism behind the impulsive realization of SPODS was discussed in terms of the bare states [63,105,136], the dressed states [63,67,105] and the Bloch vector [39]. Here we focus on the interaction of a resonant double pulse sequence with the two-state atom. Figure 21 shows simulation results for this case. The assignment of quantities is the same as in Figure 19. The pulse sequence in (a) consists of a weak prepulse followed by an intense main pulse. The prepulse has a pulse area of $\theta = \frac{\pi}{2}$ (see Equation (19)) and therefore steers the atom from its groundstate $|s\rangle$ into a state of maximum electronic coherence (see (b)). The oscillating electron density is illustrated on the top left side of the figure. The coherent charge oscillation launched by the prepulse corresponds to a dipole moment $\langle\mu\rangle(t)$ oscillating with maximum amplitude (shown in (c)). Since the dipole is driven on resonance, it follows the external driving field with a phase shift of $-\frac{\pi}{2}$. As a result the interaction energy $\langle\mathcal{V}\rangle(t)$ displayed in (d) vanishes on the time average indicating equal population of the dressed states during the prepulse. Indeed the population dynamics in (b) confirm that no selectivity is obtained throughout the prepulse. The main pulse however, being phase-shifted by $\Delta\zeta = \frac{\pi}{2}$ with respect to the prepulse, oscillates anti-phase with the induced dipole. With its onset the interaction energy is maximized abruptly. Throughout the main pulse its time average coincides with the energy of the upper dressed state indicating the selective population of the upper dressed state. This is confirmed by the dressed state population dynamics shown in (b). Remarkably, the bare state populations remain constant, i.e. locked, during the entire interaction with the main pulse – despite the presence of the strong resonant laser field. The phase configuration of field and dipole inhibits further excitation. Instead only the quantum mechanical phase of the two-state system is driven clockwise (not shown) resulting in the described enhancement of the

interaction energy. On the other hand, shifting the main pulse by $\Delta\zeta = -\frac{\pi}{2}$ with respect to the prepulse leads to in-phase oscillation of field and induced dipole. By this means the interaction energy is minimized and the lower dressed state is populated selectively. Because photoionization is triggered predominantly by the intense main pulse, only the selected dressed state is projected to the continuum resulting in the highly asymmetric AT doublets observed in Figure 20. In conclusion, driving quantum systems by phase-locked sequences of ultrashort laser pulses with carefully adjusted relative phases provides a means for efficient and ultrafast switching between the dressed states.

3.3.5   Efficient Control of Concerted Electron-Nuclear Dynamics in Molecules

In this section we extend the principles of SPODS as discussed in the previous sections from atomic prototype systems to the strong-field control of coherent electron dynamics in molecules. The basic physical mechanism behind SPODS realized by shaped femtosecond laser pulses can be summarized as follows: The initial part of the shaped pulse excites a coherent charge oscillation of maximum amplitude which is exploited by a later part of the pulse to either increase or decrease the interaction energy by tailoring the optical phase to the phase of the induced dipole oscillation. In general, the situation in molecules is more complicated than in atoms, due to the coupling between electronic and nuclear degrees of freedom. Vibrational dynamics launched along with the electronic excitation affect both the amplitude and the phase of the induced charge oscillation. A maximum amplitude of the electric dipole oscillation, required for complete selectivity, is obtained only for a maximum overlap of the nuclear wave packets in the ground and excited state. The propagation of nuclear wave packets may thus impede the build-up of the dipole oscillation. Moreover, the wave packet propagation leads to a continuous variation of the electronic resonance, changing the frequency of the electric dipole. This results in an additional phase drift which the laser field has to adapt to in order to maintain a defined phase relation to the dipole. Therefore, simple pulse shapes such as doublepulse sequences or linearly chirped pulses are not expected to be optimal for the efficient control of coupled electron-nuclear dynamics in
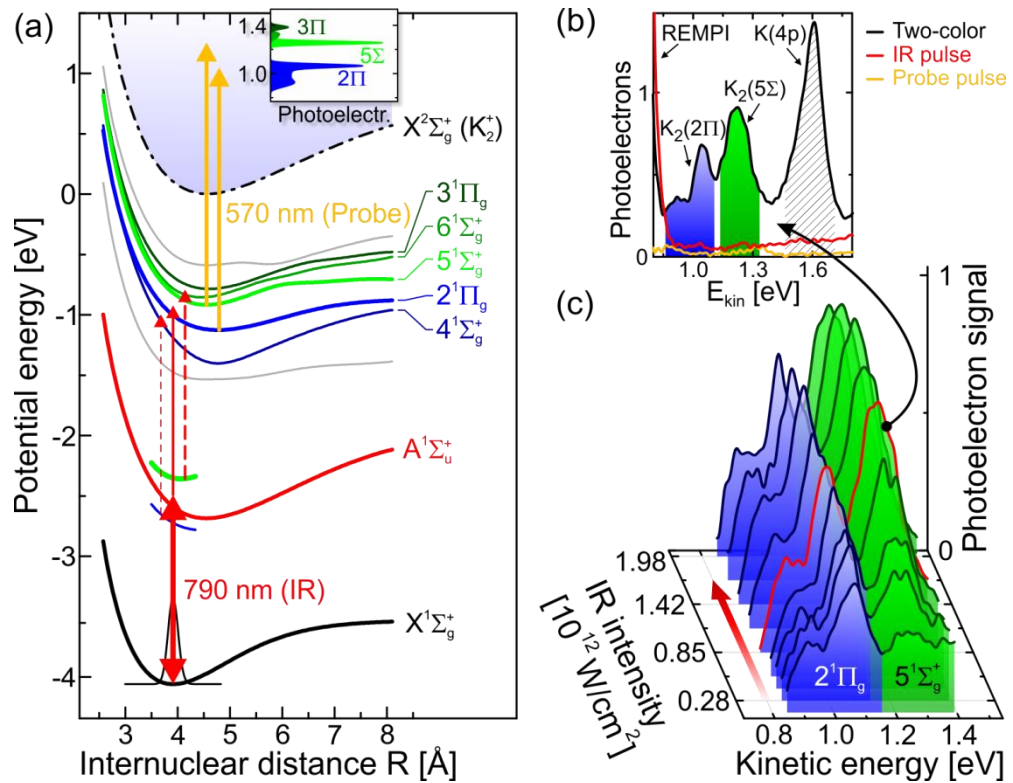
molecules.

Figure 22 Two-color excitation and ionization of K_2 molecules. (a) Potential energy scheme of K_2 excited by infrared (IR) pump pulses and post-ionized by visible probe pulses. The short blue and green lines indicate the dressed states of the X-A-subsystem, arising under strong-field excitation of K_2. (b) Two-color photoelectron spectrum recorded with the bandwidthlimited IR pulse. The choice of the probe wavelength ensures background-free detection of molecular signals from the target states $2^1\Pi_g$ and $5^1\Sigma_g^+$. (c) Intensity study of the neutral excitation by the bandwidth limited IR pulse. In the weak-field regime only the lower target state $2^1\Pi_g$ is excited. Above a threshold intensity of 0.5×10^{12} W/cm2 the upper target state $5^1\Sigma_g^+$ becomes energetically accessible as well and is populated efficiently.

In [69] complex shaped pulses from sinusoidal phase modulation were used for ultrafast switching of electronic excitation between different target channels in a neutral molecule. In this work the potassium molecule K_2 was chosen as a model system because it can be treated on a highly accurate level both experimentally and theoretically. The ground state transition $A^1\Sigma_u^+ \leftarrow X^1\Sigma_g^+$ is near-resonant with the spectrum of typical infrared (IR) femtosecond lasers, and the molecule exhibits a set of high-lying neutral target states for selective

excitation. Figure 22(a) shows the potential energy scheme of K_2 excited by $\lambda_0 = 790$ nm laser pulses with an intensity FWHM of 25 fs, and photoionized by a second delayed laser pulse centered at $\lambda_p = 570$ nm. The probe pulse maps the final population of the target states $2^1\Pi_g$ and $5^1\Sigma_g^+$ into the photoelectron spectrum. Its central wavelength was chosen to ensure background free detection of the relevant two-color photoelectron signals (cf. Figure 22(b)). In the weak-field regime only the target state $2^1\Pi_g$ is excited by a resonant two-photon absorption process from the ground state $X^1\Sigma_g^+$ via the intermediate state $A^1\Sigma_u^+$. The corresponding two-color photoelectron spectrum is displayed at the front of Figure 22(c). It shows a weak contribution from the $2^1\Pi_g$ state around $E_{kin} = 1.0$ eV and almost no electrons from the $5^1\Sigma_g^+$ state. All spectra in Figure 22(c) are recorded using a bandwidth-limited IR pulse. Only with increasing IR laser intensity the upper target state $5^1\Sigma_g^+$ becomes accessible as well due to the increased dressed state energy splitting in the resonant X-A-subsystem. Hence the steep rise of the $5^1\Sigma_g^+$-contribution around $E_{kin} = 1.25$ eV observed in Figure 22(c) as the IR intensity grows. At the intensity $I_0 = 8.5 \times 10^{11}$ W/cm² the $5^1\Sigma_g^+$ signal already dominates the spectrum indicating more efficient population of the upper target state as compared to the lower target state $2^1\Pi_g$ by the unshaped pulse. The reason for this asymmetry is a slight blue-detuning of the IR laser spectrum with respect to the X-A-resonance. Due to this detuning the induced dipole tends to oscillate in anti-phase with the driving laser field already upon creation, favouring the upper dressed state and thus biasing the system towards the upper target channel. However, by specific tailoring of the IR excitation pulse using, e.g., sinusoidal spectral phase modulation (cf. Equation (45)) the influence of the detuning can be compensated effectively. The two-color spectrum shown on the left side of Figure 23(a) was recorded with the same pulse energy but making use of sinusoidal spectral phase modulation with $A = 0.8$ rad, $T = 45$ fs and $\phi = 1.8$ rad. The $2^1\Pi_g$ contribution is strongly enhanced at the expense of the $5^1\Sigma_g^+$ contribution, indicating the efficient and selective population of the $2^1\Pi_g$ state by the shaped IR pulse. The dashed lines represent calculated photoelectron spectra based on quantum dynamics simulations described in detail in [29].
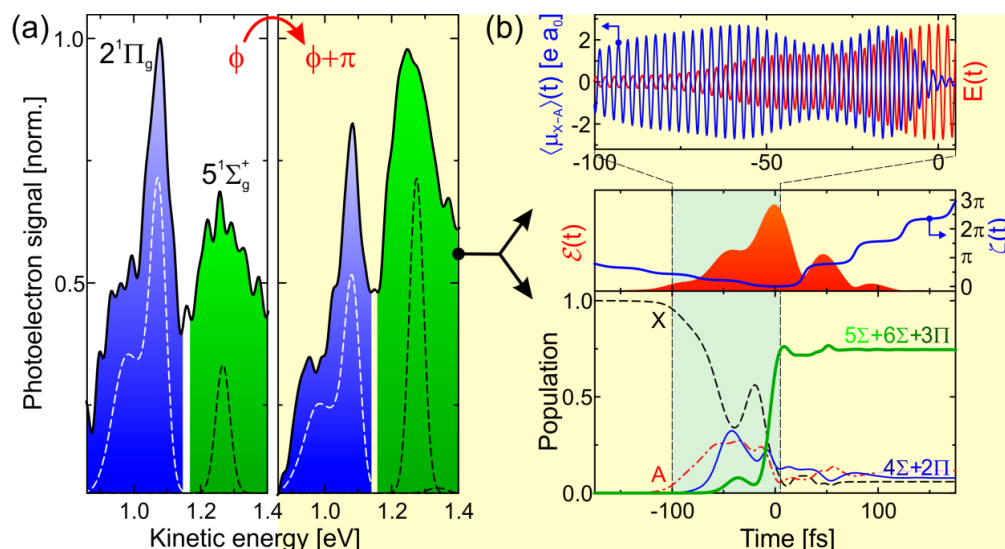
Figure 23 Control of coupled electron-nuclear dynamics in K_2 by sinusoidally phase shaped laser pulses. (a) Two-color spectra indicating efficient and selective population of the lower target state $2^1\Pi_g$ (left frame) and upper target state $5^1\Sigma_g^+$ (right frame), respectively. The two cases differ only in the applied sine-phases ϕ, which changes by π from left to right. (b) Simulated quantum dynamics behind the right spectrum in (a). The lower frame shows the neutral population dynamics of the relevant molecular states. The middle frame shows the shaped laser pulse decomposed into its amplitude (red background) and phase (blue line). The top frame illustrates the induced dipole moment (blue line) and its phase relation to the real-valued, i.e. fast oscillating laser electric field during the relevant switching time window.

The simulations confirm, that the shaped pulse not only breaks the anti-phase relation to the induced charge oscillation but succeeds to establish an in-phase oscillation to steer the molecule efficiently into the lower target channel. On the other hand, changing the sine phase ϕ by approximately π results in the spectrum shown on the right side of Figure 23(a). Here the $5^1\Sigma_g^+$ signal is strongly enhanced even beyond that obtained with the bandwidth limited pulse. The corresponding simulation results for the neutral molecular dynamics driven by the shaped pulse are presented in Figure 23(b). In the relevant time window between $t = -100$ fs and 0 fs the pulse steers the X- A -subsystem into a coherent superposition and launches the charge oscillation (blue line in the top frame). The dipole is initiated almost in anti-phase configuration to the laser field. This phase relation is further optimized during the rising edge of the shaped pulse until both oscillate perfectly out-of-phase, maximizing the

interaction energy. Therefore, as soon as the most intense part of the pulse opens the upper target channel energetically (around $t = 0$) the population flows efficiently and selectively from the X-A-subsystem into the upper target states. Finally a total population yield of 75% is obtained in the upper target channel while the lower target channel receives only 8% of population. A detailed analysis of the vibrational dynamics during the build-up of the coherence and the switching of population into the upper target channel reveals an increase of the internuclear distance by 8% which corresponds to a change of the Bohr frequency in the X-A-subsystem of 100 meV.

In conclusion, specific shaping of the temporal amplitude and phase of an intemse ultrashort laser pulse enables efficient control of the coupled electron-nuclear dynamics in molecules. Tailoring the intricate interplay between the driven charge oscillation and the driving laser field, by adapting the optical phase to the induced charge dynamics and introducing directed energy shifts via the field amplitude, provides an avenue to steer the system selectively into predefined target channels that may even be completely inaccessible in the case of weak-field excitation.

4   Control of ionization processes in dielectrics

In this last chapter we shortly highlight the extension of experimental control methodologies to ultrafast laser control of incoherent processes with an emphasis on processing of dielectrics on the nanometer scale. Here, primary processes induced by ultrafast laser radiation involve nonlinear electronic excitation where electron-electron collisions at high excitation densities (in the range 10^{21} cm^{-3} for ablation of dielectrics) destroy any coherence imprinted by the light field. In general, the electronic excitation is followed by energy transfer to the lattice and phase transitions that occur on fast (femtosecond to picosecond) but material dependent time scales [137,138]. Optimal energy coupling with the help of suitably shaped temporal pulse envelopes gives thus the possibility to guide the material response towards user-designed directions, offering extended flexibility for quality material processing [20].

Prototype studies in the above mentioned spirit have been performed on dielectrics,

water and metals. For dielectrics a microscope objective was used to obtain a focal spot with a calculated and measured diameter of 1.4 µm (see Figure 24(a)). Different thresholds for material processing with temporally asymmetric pulse shapes were observed (see Figure 24(b)) which is attributed to control of different ionization processes i.e. multi photon ionization (MPI) and avalanche ionization (AI) [58,59,139,140].
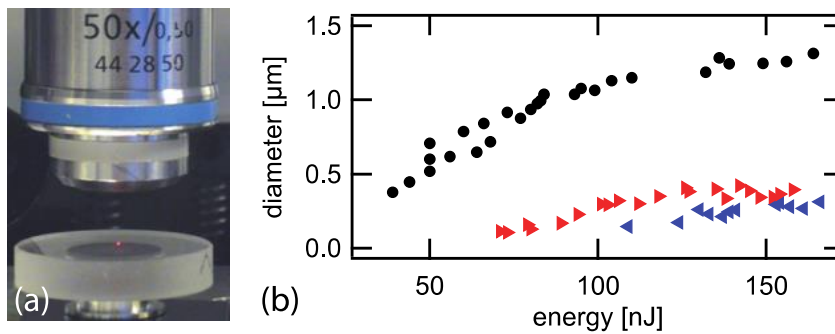

Figure 24: (a) In the materials processing platform, a femtosecond laser pulse is focused with a microscope objective. The Zeiss LD Epiplan 50x/0.5 NA objective delivers a calculated and measured spot diameter of 1.4 µm (1/e^2 value of intensity profile). Due to the nonlinear interaction the laser induced plasma is highly localized. (b)Diameters of ablation structures measured by scanning electron microscopy (SEM)for fused silica for zero, positive and negative TOD modulations (black circles for ϕ_3 = 0 fs^3, red triangles for ϕ_3 = +6 x 10^5 fs^{3}and blue triangles for ϕ_3 = -6 x 10^5 fs^3).

An exemplification of the transient free electron dynamics for unshaped and TOD-shaped pulses used in this experiment is shown in Figure 25. The free electron density n_e is modeled by a single rate equation dn_e/dt = $\sigma_k I^k$ + $\alpha n_e I$ implementing multi photon ionization (MPI) with coefficient σ_k and avalanche ionization (AI) with coefficient α. As MPI is a k-photon process and therefore most efficient at high intensities (e. g. unshaped pulses in the middle row of Figure 25). AI on the other hand needs an initial free electron population and time to work efficient. Negative TOD results in a train of sub-pulses with increasing intensity. Up to the last few sub-pulses the intensity is too low for efficient MPI and the transient free electron density is insufficient for efficient AI (see Figure 25 top). On the other hand positive TOD gives a train of sub-pulses with decreasing intensities which leads to efficient MPI at the beginning and therefore a sufficient initial free electron density which is efficiently amplified by AI (see Figure 25 bottom).Note that for laser pulses with the same energy the free electron density

exceeds the critical value for material ablation n_c for a positive TOD but not for negative TOD. This observation has been discussed in a *seed and heat* mechanism based on a refined ionization model employing a multiple rate equation approach [58].
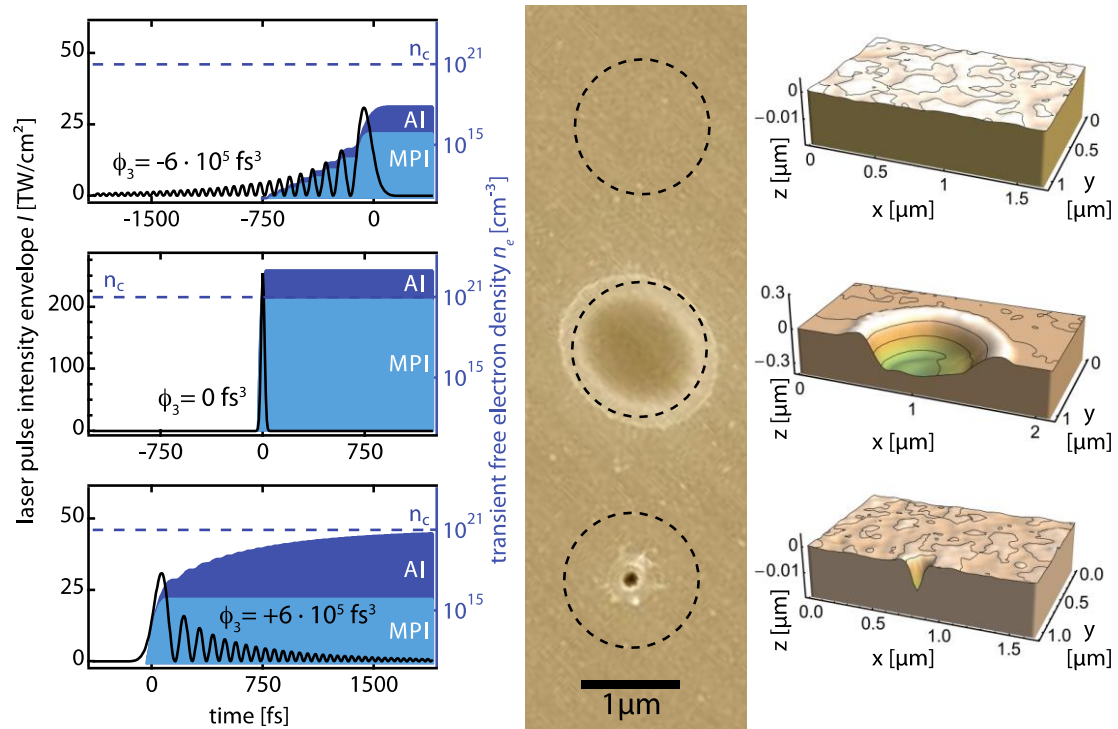

Figure 25: Control of ionization processes in fused silica via asymmetrically shaped femtosecond pulses for three TOD parameters (top row: negative TOD with ϕ_3 = -6 x 10^5 fs^3, middle row: zero TOD with ϕ_3 = 0 fs^3, and bottom row: positive TOD with ϕ_3 = +6 x 10^5 fs^3) at the same laser pulse energy. The left column shows the temporal profile of pulse intensity envelope (solid black line) and transient free electron density (light blue: contribution from multiphoton ionization (MPI) only, dark blue: contribution from avalanche ionization (AI) in combination with MPI). The critical electron density n_c = 10^{21} cm^{-3} resulting in ablation is marked with a dashed line. The middle column shows scanning electron microscope (SEM) micrographs including a dashed circle for the calculated and measured spot diameter of 1.4 µm ($1/e^2$ value of intensity profile) and the middle column shows the corresponding atomic force (AFM) micrographs (note the different z-scaling for middle row).

The resulting nanometer scale structures were measured by AFM and SEM and are one order of magnitude below the diffraction limit (see Figure 25). Recently the studies on the dynamics of the free electron plasma created by femtosecond pulses in a thin water jet [141,142] were extended to a direct observation of the free electron density after excitation with temporally shaped laser pulses by using spectral interference

techniques [143,144]. Employing this technique allowed to directly confirm control of the two ionization mechanisms in the low excitation regime making use of a Drude model and the justified assumption of homogenous excitation within the laser excited volume. The high excitation regime is in the focus of current research.

Regarding the nanoscale structures created with temporally shaped laser pulses in solid dielectrics, the physical picture is still not conclusive[140]. On a first glance the small structures might be attributed to filamentation processes as observed in bulk fused silica under similar excitation conditions [145] as well as on surfaces of dielectrics [146,147] and reviewed in[148]. However, as filamentation usually needs propagation to occur, the lack of observed propagation structures especially for the TOD shaped pulses may rule out filamentation as the only explanation. While the seed and heat model explains the threshold dependence on the temporally asymmetric pulse shapes, the spatial observations require further extensions to the simulation model. The motivation stems from the simple picture that an initial part of the pulse structure may create free electrons in a spatially very confined region well below the damage threshold via MPI and the remaining pulse exploits AI to reach the critical energy also in a very restricted area. In that simulations rate equations were solved for a Gaussian spatial beam profile taking MPI, AI and recombination into account as a function of various temporal profiles. So far, these simulations did not arrive at a conclusive picture. Currently it is speculated in addition, to what extent nanoplasmonic effects [149] like for example near field effects from a spatially confined region of high electron densities created by a part of the temporal structured laser pulse can also be responsible for part of the observations. Within the context of near field enhancements it has been shown, that by exploiting polarization dependent near field effects[78] nanoscale material processing of dielectrics can be achieved [150-152].

As mentioned above shortly, laser electron excitation with ultrashort laserpulses is followed by electron thermalization on a femtosecond time scale and coupling to the lattice on a femtosecond to picosecond time scale. Finally a free ablation plume is observed on a picosecond to nanosecond time scale that contains spectrochemical information on the ablated material. This laser-induced breakdown spectroscopy (LIBS)

is a well-established technique for spectrochemical element analysis in various applications [153,154]. Although LIBS does not achieve the sensitivity of other methods, as for example mass spectrometry, to date it offers a wide range of different advantages: No special sample preparation is needed and the analysis can be done in air under atmospheric conditions. Usually nanosecond lasers are used in these applications. Femtosecond laser pulses on the other hand offer due to different ablation processes a more precise ablation with less thermal damage and with a higher reproducibility compared to nanosecond pulses [155]. Furthermore the femtosecond laser-induced plasma features a faster temporal decay and a reduced background[156], enabling to work at a higher repetition rate without any gate for data acquisition. On this basis femtosecond laser pulses are suitable to improve the spatial resolution and spectrochemical sensitivity in comparison to ns-LIBS and facilitate fs-LIBS for biomedical applications [157], such as chemical mapping[158] and depth profiling of complex biological systems[156]. In order to minimize the spatial structure and at the same time maximize the spectrochemical sensitivity for fs-LIBS temporal pulse tailoring was exploited for material processing: by applying double pulses an increase in line specific emission was observed, and spatial resolution of few µm and below have been achieved [159].

5   Summary and Conclusion

In this review we have presented an overview on recent work on control of ultrafast electron dynamics using shaped femtosecond laser pulses with applications ranging from the manipulation of a single electron in order to create a designer electron wave packet to macroscopic control of electron densities in femtosecond materials processing.

Shaped femtosecond laser pulses are an outstanding tool to manipulate molecular dynamics. Therefore, an introduction to the fundamentals of femtosecond pulse shaping including polarization shaping was presented in view of the applications discussed in this review. Because the physical basis of coherent control is the manipulation of the interferences of matter waves, the coherence transfer from shaped pulses to matter waves was discussed in some detail. As an example for three-

dimensional control with polarization-shaped pulses we have studied the creation and detection of designer electron wave packets. It turned out that the underlying physical mechanism is based on the creation of superposition states in the continuum by the interplay between the time-dependent polarization of the laser pulse and the respective complex-valued transition matrix elements as well as the subsequent interference of the partial electron wave packets in the continuum.

Non-perturbative interaction with shaped intense laser fields enables new control scenarios and allows efficient population transfer to the target states. We have considered prototypical examples of strong-field control which highlight specific physical mechanisms of non-perturbative control, such as Dynamic Stark shifts (DSS) and Selective Population of Dressed States (SPODS). The analysis of dressed states populations and energies proved to be particularly suitable to analyze strong-field control. We showed that the concept of (SPODS) provides a unifying framework to describe adiabatic techniques such as Rapid Adiabatic passage (RAP) and non-adiabatic control enabling ultrafast switching. As a topical example for strong field control we have discussed the manipulation of concerted nuclear-electron dynamics in molecules by shaped intense laser pulses. Tailoring the laser field to the induced charge oscillation in a molecule turned out to be a general theme in coherent control of electron dynamics.

The enduring progress in the refinement of femtosecond laser sources in terms of tunability, pulse-width (associated with increasing bandwidth) and CEP stabilization opens new perspectives for coherent control of ultrafast dynamics. For instance, due to the decrease of the pulse duration, faster and faster processes such as electron dynamics will come to the fore. In addition, control by the carrier envelope phase (CEP) will become increasingly important in this regime - especially for highly non-linear processes. Along with the trend towards shorter pulses goes the broadening of the laser bandwidth promising a much higher degree of attainable control because all molecular degrees of freedom become accessible simultaneously. Furthermore, ultrafast light sources being tunable over a wide spectral band will broaden the range of applications by tailoring the laser central frequency with respect to the application

rather than selecting the application based on the available frequencies. Extending recent efforts on the generation and characterization of shaped femtosecond laser pulses in the ultraviolet towards XUV- and X-ray sources should in principle be feasible by combining dispersive elements with absorbing targets. Due to the Kramers-Kronig relation for dielectric functions the insertion of absorbing targets will also include dispersive effects enabling amplitude and phase control. Based on these innovative developments we anticipate a huge variety of novel experiments and applications in coherent control.

6   Acknowledgement

Reference List

[1] S. A. Rice and M. Zhao, in *Optical control of molecular dynamics*, (Wiley, New York, 2000).
[2] M. Shapiro and P. Brumer, in *Principles of the Quantum Control of Molecular Processes*, 1 ed., (John Wiley & Sons, Hoboken, New Jersey, 2003).
[3] D. Tannor, in *Introduction to Quantum Mechanics: A Time-Dependent Perspective*, (Palgrave Macmillan Publishers Limited, Houndmills, Basingstoke, Hampshire, RG21 6XS, England, 2007).
[4] D. J. Tannor and S. A. Rice, Adv Chem Phys **70,** 441 (1988).
[5] M. Shapiro and P. Brumer, Int Rev Phys Chem **13,** 187 (1994).
[6] T. Baumert, J. Helbing, and G. Gerber, in *Advances in Chemical Physics - Photochemistry: Chemical Reactions and their control on the Femtosecond Time Scale*, Edited by I. Prigogine and S. A. Rice (John Wiley & Sons, Inc., New York, 1997).
[7] H. Rabitz, R. de Vivie-Riedle, M. Motzkus, and K. Kompa, Science **288,** 824 (2000).
[8] M. Shapiro and P. Brumer, Rep Prog Phys **66,** 859 (2003).
[9] D. Goswami, Phys Rep **374,** 385 (2003).
[10] M. Dantus and V. V. Lozovoy, Chem Rev **104,** 1813 (2004).
[11] V. Bonacic-Koutecky and R. Mitric, Chem Rev **105,** 11 (2005).
[12] T. Brixner *et al.*, in *Femtosecond Laser Spectroscopy*, Edited by P. Hannaford (Springer Verlag, 2005), Chap. 9.
[13] M. Wollenhaupt, V. Engel, and T. Baumert, Ann Rev Phys Chem **56,** 25 (2005).
[14] P. Nuernberger, G. Vogt, T. Brixner, and G. Gerber, Phys Chem Chem Phys **9,** 2470 (2007).
[15] J. Werschnik and E. K. U. Gross, J Phys B **40,** R175-R211 (2007).
[16] W. Wohlleben, T. Buckup, J. L. Herek, and M. Motzkus, Chem Phys Chem **6,** 850 (2005).
[17] Y. Silberberg, Ann Rev Phys Chem **60,** 277 (2009).
[18] K. Ohmori, Ann Rev Phys Chem **60,** 487 (2009).
[19] C. Brif, R. Chakrabarti, and H. Rabitz, New J Phys **12,** 075008 (2010).
[20] R. Stoian, M. Wollenhaupt, T. Baumert, and I. V. Hertel, in *Laser Precision Microfabrication*, Edited by K. Sugioka, M. Meunier, and A. Piqué (Springer-Verlag, Berlin Heidelberg, 2010), Chap. 5.
[21] M. Wollenhaupt and T. Baumert, Faraday Discuss **153,** 9 (2011).
[22] M. Wollenhaupt, C. Lux, M. Krug, and T. Baumert, Chem Phys Chem **14,** 1341 (2013).
[23] S. Thallmair *et al.*, in *Molecular quantum dynamics – from theory to applications*, Edited by F. Gatti (Springer, 2014).
[24]   Edited by P. Gaspard and I. Burghardt (John Wiley, New York, 1997), Chap. 101.
[25] J. L. Herek, J Photochem Photobiol A **180,** 225 (2006).
[26] H. Fielding, M. Shapiro, and T. Baumert, J Phys B **41,** 070201-1 (2008).
[27] H. Rabitz, New J Phys **11,** 105030 (2009).
[28] H. H. Fielding and M. A. Robb, Phys Chem Chem Phys **12,** 15569 (2010).
[29] H. Braun *et al.*, Journal of Physics B **47,** 124015 (2014).
[30] M. Wollenhaupt, A. Assion, and T. Baumert, in *Springer Handbook of Lasers and Optics*, 2 ed., Edited by F. Träger (Springer, Dordrecht Heidelberg London New York, 2012), Chap. 12.
[31] A. Monmayrant, S. Weber, and B. Chatel, J Phys B : At Mol Opt Phys **43,** 103001-34 (2010).
[32] J. Schneider *et al.*, Phys Chem Chem Phys **13,** 8733 (2011).
[33] A. Galler and T. Feurer, Appl Phys B **90,** 427 (2008).
[34] B. von Vacano, T. Buckup, and M. Motzkus, J Opt Soc Am B **24,** 1091 (2007).
[35] J. Köhler *et al.*, Opt Express **19,** 11638 (2011).

[36] R. Bracewell, in *The Fourier Transform and Its Applications*, 3rd ed., (McGraw-Hill Higher Education, Singapore, 2000).
[37] L. Allen and J. H. Eberly, in *Optical Resonance and Two-Level Atoms*, 2nd ed., (Dover Publications, New York, 1987).
[38] N. Dudovich, T. Polack, A. Pe´er, and Y. Silberberg, Phys Rev Lett **94,** 083002-4 (2005).
[39] M. Wollenhaupt *et al.*, Phys Rev A **73,** 063409-15 (2006).
[40] T. Bayer, M. Wollenhaupt, and T. Baumert, J Phys B **41,** 074007-13 (2008).
[41] L. Cohen, in *Time-Frequency Analysis*, (Prentice Hall PTR, New Jersey, 1995).
[42] E. Sorokin, G. Tempea, and T. Brabec, JOSA B **17,** 146 (2000).
[43] A. Präkelt, M. Wollenhaupt, C. Sarpe-Tudoran, and T. Baumert, Phys Rev A **70,** 063407-10 (2004).
[44] H. R. Telle *et al.*, Appl Phys B **69,** 327 (1999).
[45] F. W. Helbing *et al.*, Appl Phys B **74,** 35 (2002).
[46] A. Apolonski *et al.*, Phys Rev Lett **92,** 073902-4 (2004).
[47] G. Sansone *et al.*, Phys Rev A **73,** 053408 (2006).
[48] M. F. Kling *et al.*, New J Phys **10,** 025024-17 (2008).
[49] G. Cerullo, A. Baltuska, O. D. Mucke, and C. Vozzi, Laser & Photonics Reviews **5,** 323 (2011).
[50] B. Broers, L. D. Noordam, and H. B. van Linden van den Heuvell, Phys Rev A **46,** 2749 (1992).
[51] C. J. Bardeen, Q. Wang, and C. V. Shank, Phys Rev Lett **75,** 3410 (1995).
[52] A. Assion *et al.*, Chem Phys Lett **259,** 488 (1996).
[53] J. Degert *et al.*, Phys Rev Lett **89,** 203003-203003-4 (2002).
[54] M. Wollenhaupt *et al.*, Appl Phys B **82,** 183 (2006).
[55] P. Nuernberger, Opt Comm **282,** 227 (2009).
[56] M. Krug *et al.*, New J Phys **11,** 105051 (2009).
[57] J. D. McMullen, JOSA **67,** 1575 (1977).
[58] L. Englert *et al.*, Opt Express **15,** 17855 (2007).
[59] L. Englert *et al.*, Appl Phys A **92,** 749 (2008).
[60] N. T. Form, B. J. Whitaker, and C. Meier, J Phys B : At Mol Opt Phys **41,** 074011 (2008).
[61] M. Ruge *et al.*, J Phys Chem C **117,** 11780 (2013).
[62] D. Meshulach and Y. Silberberg, Nature **396,** 239 (1998).
[63] M. Wollenhaupt *et al.*, J Mod Opt **52,** 2187 (2005).
[64] A. Bartelt *et al.*, Phys Chem Chem Phys **5,** 3610 (2003).
[65] V. V. Lozovoy, I. Pastirk, A. Walowicz, and M. Dantus, J Chem Phys **118,** 3187 (2003).
[66] M. Wollenhaupt and T. Baumert, J Photochem Photobiol A **180,** 248 (2006).
[67] M. Wollenhaupt *et al.*, Chem Phys Lett **419,** 184 (2006).
[68] J. L. Herek *et al.*, Nature **417,** 533 (2002).
[69] T. Bayer *et al.*, Phys Rev Lett **110,** 123003 (2013).
[70] N. Dudovich, D. Oron, and Y. Silberberg, J Chem Phys **118,** 9208 (2003).
[71] J. Voll and R. Vivie-Riedle, New Journal of Physics **11,** 105036 (2009).
[72] J. Hauer, T. Buckup, and M. Motzkus, J Chem Phys **125,** 061101-3 (2006).
[73] T. Brixner and G. Gerber, Opt Lett **26,** 557 (2001).
[74] N. Dudovich, D. Oron, and Y. Silberberg, Phys Rev Lett **92,** 103003-4 (2004).
[75] T. Brixner *et al.*, Phys Rev Lett **92,** 208301-4 (2004).
[76] M. Wollenhaupt *et al.*, Appl Phys B **95,** 245 (2009).
[77] F. Weise, G. Achazi, and A. Lindinger, Phys Chem Chem Phys **13,** 8621 (2011).
[78] M. Aeschlimann *et al.*, Nature **446,** 301 (2007).
[79] P. Schön *et al.*, Phys Rev A **81,** 013809 (2010).
[80] R. Selle *et al.*, Opt Lett **33,** 803 (2008).
[81] A. M. Weiner, Rev Sci Instr **71,** 1929 (2000).
[82] A. Präkelt *et al.*, Rev Sci Instr **74,** 4950 (2003).
[83] D. B. Strasfeld, S.-H. Shim, and M. T. Zanni, Adv Chem Phys **141,** 1 (2009).
[84] T. Hornung, R. Meier, and M. Motzkus, Chem Phys Lett **326,** 445 (2000).

[85]   S. Fechner *et al.*, Opt Express **15,** 15387 (2007).
[86]   S. Ruetzel *et al.*, Phys Chem Chem Phys **13,** 8627 (2011).
[87]   R. S. Judson and H. Rabitz, Phys Rev Lett **68,** 1500 (1992).
[88]   T. Baumert *et al.*, Appl Phys B **65,** 779 (1997).
[89]   D. Meshulach, D. Yelin, and Y. Silberberg, Opt Comm **138,** 345 (1997).
[90]   C. J. Bardeen *et al.*, Chem Phys Lett **280,** 151 (1997).
[91]   A. Assion *et al.*, Science **282,** 919 (1998).
[92]   R. J. Levis and H. A. Rabitz, J Phys Chem A **106,** 6427 (2002).
[93]   C. Daniel *et al.*, Science **299,** 536 (2003).
[94]   D. Yelin, D. Meshulach, and Y. Silberberg, Opt Lett **22,** 1793 (1997).
[95]   N. Hansen, in *The CMA Evolution Strategy: A Tutorial*, 2009).
[96]   J. W. Wilson *et al.*, Rev Sci Instrum **79,** 033103-5 (2008).
[97]   M. Wollenhaupt *et al.*, Phys Rev Lett **89,** 173001-4 (2002).
[98]   F. Lindner *et al.*, Phys Rev Lett **95,** 040401-4 (2005).
[99]   M. Winter, M. Wollenhaupt, and T. Baumert, Optics Communications **264,** 285 (2006).
[100]   P. B. Corkum and F. Krausz, Nature Physics **3,** 381 (2007).
[101]   J. Mauritsson *et al.*, Phys Rev Lett **105,** 053001 (2010).
[102]   M. Born, Phys Bl **2,** 49 (1955).
[103]   C. Cohen-Tannoudji, B. Diu, and F. Laloe, in *Quantum Mechanics Volume 1*, (John Wiley & Sons, 1977).
[104]   P. Brumer and M. Shapiro, Annual Review of Physical Chemistry **43,** 257 (1992).
[105]   M. Wollenhaupt *et al.*, J Opt B **7,** S270-S276 (2005).
[106]   M. Wollenhaupt, M. Krug, and T. Baumert, Phys Journ **11,** 37 (2012).
[107]   P. Hockett, M. Wollenhaupt, C. Lux, and T. Baumert, Phys Rev Lett **112,** 223001 (2014).
[108]   K. L. Reid, Mol Phys **110,** 131 (2012).
[109]   M. Wollenhaupt *et al.*, Appl Phys B **95,** 647 (2009).
[110]   D. A. Malik *et al.*, Phys Rev A **84,** 043404-043404-5 (2011).
[111]   A. Vredenborg *et al.*, Chem Phys Chem **12,** 1459 (2011).
[112]   J. Maurer *et al.*, Phys Rev Lett **109,** 123001 (2012).
[113]   A. T. J. B. Eppink and D. H. Parker, Rev Sci Instr **68,** 3477 (1997).
[114]   in *Imaging in Molecular Dyanmics - Technology and Applications*, (Cambridge, 2003).
[115]   G. A. Garcia, L. Nahon, and I. Powis, Rev Sci Instr **75,** 4989 (2004).
[116]   A. C. Kak and M. Slaney, in *Principles of Computerized Tomographic Imaging*, (IEEE Press, 1999).
[117]   C. Smeenk *et al.*, J Phys B **42,** 165402 (2009).
[118]   P. Hockett, M. Staniforth, and K. L. Reid, Molecular Physics **108,** 1045 (2010).
[119]   T. Frohnmeyer, M. Hofmann, M. Strehle, and T. Baumert, Chem Phys Lett **312,** 447 (1999).
[120]   C. Trallero-Herrero, J. L. Cohen, and T. Weinacht, Phys Rev Lett **96,** 063603-4 (2006).
[121]   B. J. Sussman, D. Townsend, M. Y. Ivanov, and A. Stolow, Science **314,** 278 (2006).
[122]   U. Gaubatz *et al.*, Chem Phys Lett **149,** 463 (1988).
[123]   N. V. Vitanov, T. Halfmann, B. W. Shore, and K. Bergmann, Ann Rev Phys Chem **52,** 763 (2001).
[124]   B. W. Shore, acta physica slovaca **58,** 243 (2008).
[125]   E. T. Sleva, I. M. Xavier Jr., and A. H. Zewail, JOSA B **3,** 483 (1985).
[126]   Y. S. Bai, A. G. Yodh, and T. W. Mossberg, Phys Rev Lett **55,** 1277 (1985).
[127]   R. Kosloff, A. D. Hammerich, and D. Tannor, Phys Rev Lett **69,** 2172 (1992).
[128]   V. S. Malinovsky, C. Meier, and D. J. Tannor, Chem Phys **221,** 67 (1997).
[129]   S. R. Hartmann and E. L. Hahn, Phys Rev **128,** 2053 (1962).
[130]   A. Abragam, in *The Principles of Nuclear Magnetism*, 13 ed., (Clarendon Press (Reprint), 1994).
[131]   S. H. Autler and C. H. Townes, Phys Rev **100,** 703 (1955).
[132]   P. Balling, D. J. Maas, and L. D. Noordam, Phys Rev A **50,** 4276 (1994).
[133]   A. A. Rangelov *et al.*, Phys Rev A **72,** 053403-12 (2005).

[134]   J. Cao, C. J. Bardeen, and K. R. Wilson, Phys Rev Lett **80,** 1406 (1998).

[135]   V. S. Malinovsky and J. L. Krause, Eur Phys J D **14,** 147 (2001).

[136]   M. Wollenhaupt *et al.*, Phys Rev A **68,** 015401-4 (2003).

[137]   B. Rethfeld, K. Sokolowski-Tinten, D. von der Linde, and S. I. Anisimov, Appl Phys A **79,** 767 (2004).

[138]   P. Balling and J. Schou, Reports on Progress in Physics **76,** 036502 (2013).

[139]   M. Wollenhaupt, L. Englert, A. Horn, and T. Baumert, J Laser Micro Nano **4,** 144 (2009).

[140]   L. Englert *et al.*, J Laser Appl **24,** 042002-042002-5 (2012).

[141]   C. Sarpe-Tudoran *et al.*, Appl Phys Lett **88,** 261109-3 (2006).

[142]   C. Sarpe *et al.*, New J Phys **14,** 075021 (2012).

[143]   E. Tokunaga, A. Terasaki, and T. Kobayashi, Opt Lett **17,** 1131 (1992).

[144]   V. V. Temnov *et al.*, Phys Rev Lett **97,** 237403 (2006).

[145]   A. Couairon *et al.*, Phys Rev B **71,** 125435-11 (2005).

[146]   Y. V. White *et al.*, Opt Express **16,** 14411 (2008).

[147]   B. Delobelle, F. Courvoisier, and P. Delobelle, Optics and Lasers in Engineering **48,** 616 (2009).

[148]   A. Couairon and A. Mysyrowicz, Phys Rep **441,** 47 (2007).

[149]   Th. Fennel *et al.*, Rev Mod Phys **82,** 1793 (2010).

[150]   F. Hubenthal *et al.*, Appl Phys Lett **95,** 063101-3 (2009).

[151]   R. Morarescu *et al.*, J Mater Chem **21,** 4076 (2011).

[152]   A. A. Jamali *et al.*, Appl Phys A **110,** 743 (2013).

[153]   J. D. Winefordner *et al.*, J Anal At Spectrom **19,** 1061 (2004).

[154]   E. L. Gurevich and R. Hergendorfer, Appl Spectr **61,** 233A (2007).

[155]   J. Cheng *et al.*, Optics & Laser Technology **46,** 88 (2013).

[156]   A. Assion *et al.*, Appl Phys B **77,** 391 (2003).

[157]   F. Dausinger, F. Lichtner, and H. Lubatschowski, in *Femtosecond Technology for Technical and Medical Applications*, Topics in Applied Physics ed., (Springer, Berlin Heidelberg, 2004).

[158]   W. Wessel *et al.*, Engineering Fracture Mechanics **77,** 1874 (2010).

[159]   J. Mildner *et al.*, Appl Surf Sci **302,** 291 (2014).